

LEVEL

P

IMS

INSTITUTE OF MATERIALS SCIENCE

AD A 074166

DDC FILE COPY

This document has been approved
for public release and sale; its
distribution is unlimited.

Best Available Copy

THE UNIVERSITY OF CONNECTICUT

Storrs • Connecticut

15 00 20 028

Surface Hardening by Laser Skin Melting.

P.R./Strutt

July 1979 / 66

First Yearly Progress Report No. 1

Office of Naval Research
Arlington, Virginia 22217

Contract #N00014-78-C-0580

Reproduction in whole or in part is permitted for
any purpose of the United States Government.

Distribution of this document is unlimited.

Metallurgy Department
Institute of Materials Science
University of Connecticut
Storrs, Connecticut 06268

100-120

CONTENTS

Introduction	(i)
Laser Melting and Heat Treatment of M2 Tool Steel	1
A Comparative Study of Electron Beam and Laser Melting of M2 Tool Steel	22
Microstructural Characterization of a Laser Melted High Carbon Steel	42
Laser Surface Treatment of Pseudo- Binary Fe-TiC Alloys	48

[illegible]

(i)

Introduction

The program of research sponsored by the Office of Naval Research under contract N00014-78-C-0580 for the first year of effort has covered work on five general topics, these are:

- (1) A microstructural characterization of laser melting and heat treatment of M2 tool steel,
- (2) A comparative study of electron beam and laser melting of M2 tool steel,
- (3) Microstructural characterization of a laser melted high carbon steel,
- (4) Laser surface treatment of pseudobinary Fe-TiC alloys,
- (5) Electron beam surface treatment of carbide reinforced materials.

The present report includes copies of four papers in final form on topics (1) to (4). Work on the fifth topic has been recently commenced with the objective of applying rapid surface quenching techniques to a range of tool materials varying widely in carbon content and morphology. Materials being studied include carbide rich Co-(W, Ta, Ti)C and Ni-(TiC, Mo₂C), Fe-TiC alloys with both high and low volume fraction carbide and cemented carbides with a range of matrix properties.

An important aspect of the project to date is the comparison of electron beam-glazing and laser-glazing. Laser melted specimens have been prepared by United Technologies Research Center and electron-beam melted specimens by Leybold Heraeus Vacuum Systems, Enfield Connecticut. Recently, however, a Zeiss electron beam melting unit has been installed in the Metallurgy Department at the University of Connecticut and preliminary results have already been obtained. In future work this unit will be developed to produce rapidly solidified surface areas by applying triangular waveform signals to the X-Y electromagnetic deflection coils. This type of beam deflection will also be used to produce

(ii)

single pass accurately timed scans, thereby making it possible to achieve particularly high cooling rates ($\sim 10^8 \text{ }^\circ\text{C.s}^{-1}$).

To date the comparative studies on the effect of electron beam and laser surface melting of M2 tool steel demonstrate the vast superiority of the electron beam as a directed energy source in materials processing applications. One outstanding feature is the highly efficient energy coupling between the beam and material. In the present investigation it was demonstrated that surface melting with an electron beam was ten times more efficient than with a continuous CO_2 laser. Furthermore, in a situation where the surface reflectivity is particularly high "electron beam glazing" may be as much as 25 times more efficient than "laser glazing."

As a result of the nearly idealized energy coupling between an electron beam and metal substrate the degree of surface melting remains relatively constant. This results in such highly desirable features as a uniform depth of melting, a smooth surface finish, and a highly homogeneous microstructure. Detailed microstructural examination of electron beam glazed M2 tool steel revealed an ultra refinement in grain size and a finely dispersed carbide distribution. The latter produced a hardness comparable to that obtained by laser-glazing which is significantly in excess of that attained in conventional heat treatment. It should be stressed that microstructural refinement of the grain size and the carbides is desirable in obtaining high hardness combined with good fracture toughness characteristics.

Future work will involve the basic study of electron beam laser-glazed specimen of selected iron-base alloys. There will be particular emphasis on detailed microstructural characterization using transmission electron microscopy and various analytical techniques together with a study of the underlying mechanisms. Utilizing the electron-beam facility, now being developed, it will be possible to determine the effect on surface melting of processing parameters

(iii)

(such as the beam scanning velocity) which may be varied over a wide range.

Another important aspect will be the possibility of performing actual mechanical tests on small rapidly quenched surface areas produced by a beam deflection system.

Laser Melting and Heat Treatment of M2 Tool Steel:

A Microstructural Characterization

by

Young-Won Kim*, P. R. Strutt and H. Nowotny

Metallurgy Department
University of Connecticut
Storrs, Connecticut 06268

* Now at Air Force Materials Laboratory (AFSC)
Wright-Patterson Air Force Base, Ohio 45322

ABSTRACT

Microstructural characterization and electron diffraction crystal structure determinations have been carried out on the tool steel M2. Detailed examination using optical microscopy and thin-film and replica transmission electron microscopy substantiate preliminary findings (2,3). Namely, that laser melted material has a two phase δ -ferrite/austenite matrix containing a dispersion of fine M_2C carbides together with a smaller amount of $M_{23}C_6$ carbides. Subsequent heat treatment at 560°C and 1230°C increases the hardness (to a maximum value of ~1100 V.H.N.) by carbide precipitation. In material heat treated at 560°C there is a preponderance of $M_{23}C_6$ carbides together with a small amount of M_2C carbides. In contrast, the effect of heat treatment at 1230°C is to produce material containing only MC_{1-x} type carbides with diameters in the range from 20nm to ~1 μ m.

1. INTRODUCTION

It has recently been shown that laser surface melting produces a highly refined and homogeneous microstructure in non-ferrous alloys, including the nickel-base superalloys (1). Since the technique naturally lends itself to the treatment of machine tool cutting edges Strutt et al. (2,3) investigated the characteristics of laser surface melted tool steels, specifically M2 and 440-C. In this investigation the specimen surface underwent several melting and solidification cycles by repeatedly scanning with a continuous CO₂ laser, the conditions were such that the solidification cooling rate was estimated by a heat transfer analysis (4) to be $\sim 5 \times 10^5 \text{ }^\circ\text{C} \cdot \text{s}^{-1}$.

When the laser melting method was applied to the tool steel M2 there was nearly complete carbide dissolution and retention of a substantial amount of δ -ferrite in addition to austenite. In contrast to the rather complex microstructure in M2, laser melting produced a simple coupled growth δ -ferrite/Cr₇C₃ carbide eutectic structure in 440-C. Another finding is that both M2 and 440-C hardened to a degree unattainable in conventional practice following subsequent heat treatment. This feature is intriguing since there is no microstructural evidence of martensite, hence the substantial hardness appears to arise from a distribution of fine carbides precipitated upon subsequent heat treatment.

The present study was carried out to further elucidate the initial findings on laser-melted M2 tool steel and determine microstructural changes produced by subsequent heat treatment. Specific attention is devoted to the identification of carbide particles and their distribution.

2. EXPERIMENTAL METHOD

Commercially available M2 steel was used in the present study and laser surface melting was performed on fully annealed material; the nominal composition of the alloy is given in Table I. The specimen surface was scanned with a continuous laser such that each melted region was melted and solidified only once, further details are given elsewhere (2,3). After surface melting the specimens were cross-sectioned and then observed by optical and electron microscopy; Fig. 1 shows a typical cross-sectional view of a melt region. Various solutions including Murakami's reagent, Vilella's reagent and an oxalic acid solution were used, each type selectively revealing different microstructural features. A second etch in an oxalic acid/hydrochloric acid solution was used in the preparation of carbon extraction replicas for electron diffraction studies. Thin foil electron transmission microscope observations were carried out on specimens sectioned in the upper melt region. However, specimen preparation was especially difficult since perforations occurred in the melt zone/parent material interface. Microstructural studies, employing the preceding techniques, were also carried out on laser melted specimens which were given subsequent heat treatments. Two typical heat treatments were (1) heating at 1230°C for 5 min. and quenching into liquid nitrogen, and (2) aging at 560°C three times, each for 2 hrs, following by air cooling.

3. RESULTS

Previous X-ray diffraction analysis (2) of the fully annealed M2 steel shows that δ -ferrite constitutes the matrix and that the carbides consist of mainly $M_{23}C_6$ and M_6C , and small amounts of M_2C . The average particle size of carbides, as evaluated from replica observations, is $\sim 1 \mu m$. Laser surface melting drastically changes the microstructure and physical properties, as described below.

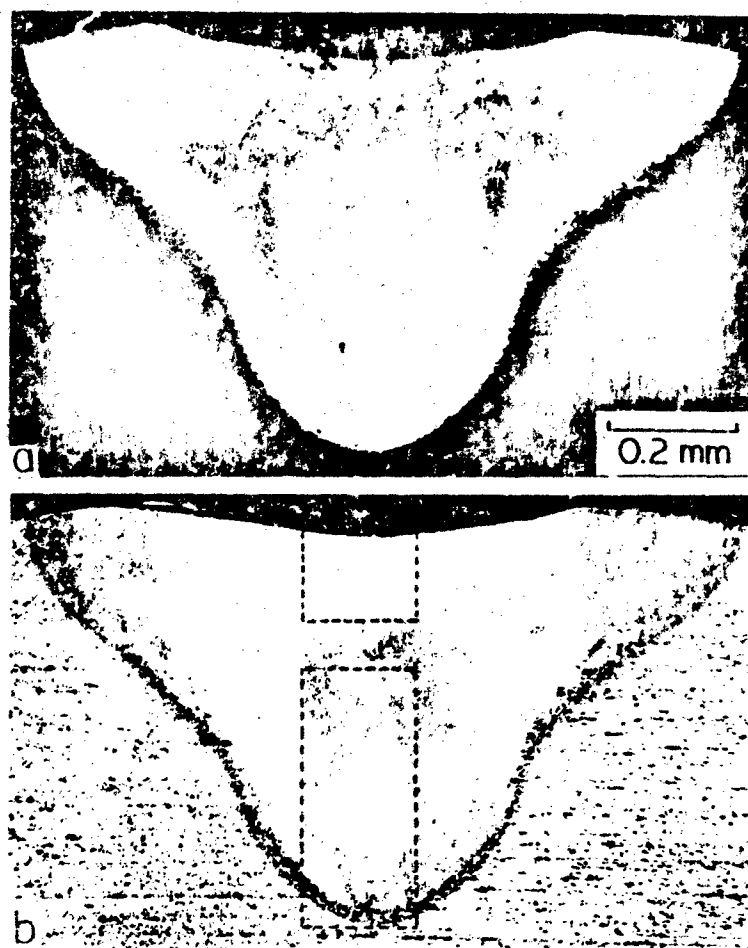


Fig. 1. Cross section of deep laser-melted region as etched with
(a) Vilella's reagent to reveal δ -regions (dark tone)
(b) Murakami's reagent to reveal austenite (dark tone)

3.1 Laser melted state

Microstructural changes throughout the melt region are shown in Fig. 2 which is an enlargement of the areas marked in Fig. 1(b). The microstructure at the maximum melt depth, Fig. 2(c), is on a very fine scale and morphologically resembles that of the chilled zone of a solidifying ingot. After the narrow chilled zone has formed, relatively long columnar dendrites grow into the melt, Fig. 2(b), and finally an equiaxed cellular structure develops in the upper melt region, Fig. 2(a). The mean interdendrite spacing, or cell diameter is from 1 to 2 μm , and on the basis of the relation of Matyja et al. (5) the cooling rate is estimated to be $\sim 10^5 \text{ }^\circ\text{C} \cdot \text{s}^{-1}$; a slightly higher rate of $\sim 5 \times 10^5 \text{ }^\circ\text{C} \cdot \text{s}^{-1}$ is deduced from a heat transfer analysis (4).

In agreement with previous studies (2,3) electron diffraction analysis of thin foil specimens shows that the upper melt region is predominantly δ -ferrite together with an amount of austenite (γ). Confirmation that the b.c.c. phase is indeed δ -ferrite is afforded by its slow transformation, in the microscope to austenite. In the dark field micrograph in Fig. 3(a) the transformed austenite is in light contrast since it was imaged with an f.c.c. reflection. The surface replica in Fig. 3(b) shows the same microstructural features as Fig. 3(a), where δ -ferrite cells are surrounded by boundaries of γ and carbides formed by the peritectic reaction $\delta + \text{liquid} \rightarrow \gamma + \text{carbide}$. A region, lower in the melt zone where the peritectic reaction has proceeded to a further stage is seen in Fig. 3(c). Since the upper melt region is predominantly δ -ferrite, and X-ray analysis (2,3) shows δ and γ are in about equal proportions when averaged over the entire melt region, the lower melt region is deduced to be essentially austenitic. The fine elongated dendrites in the austenitic lower melt zone, see Fig. 2(b and c), presumably formed as δ -ferrite which then completely transformed to austenite due to a relatively slow velocity R of the liquid/solid interface; see discussion section. It is worth noting that insight

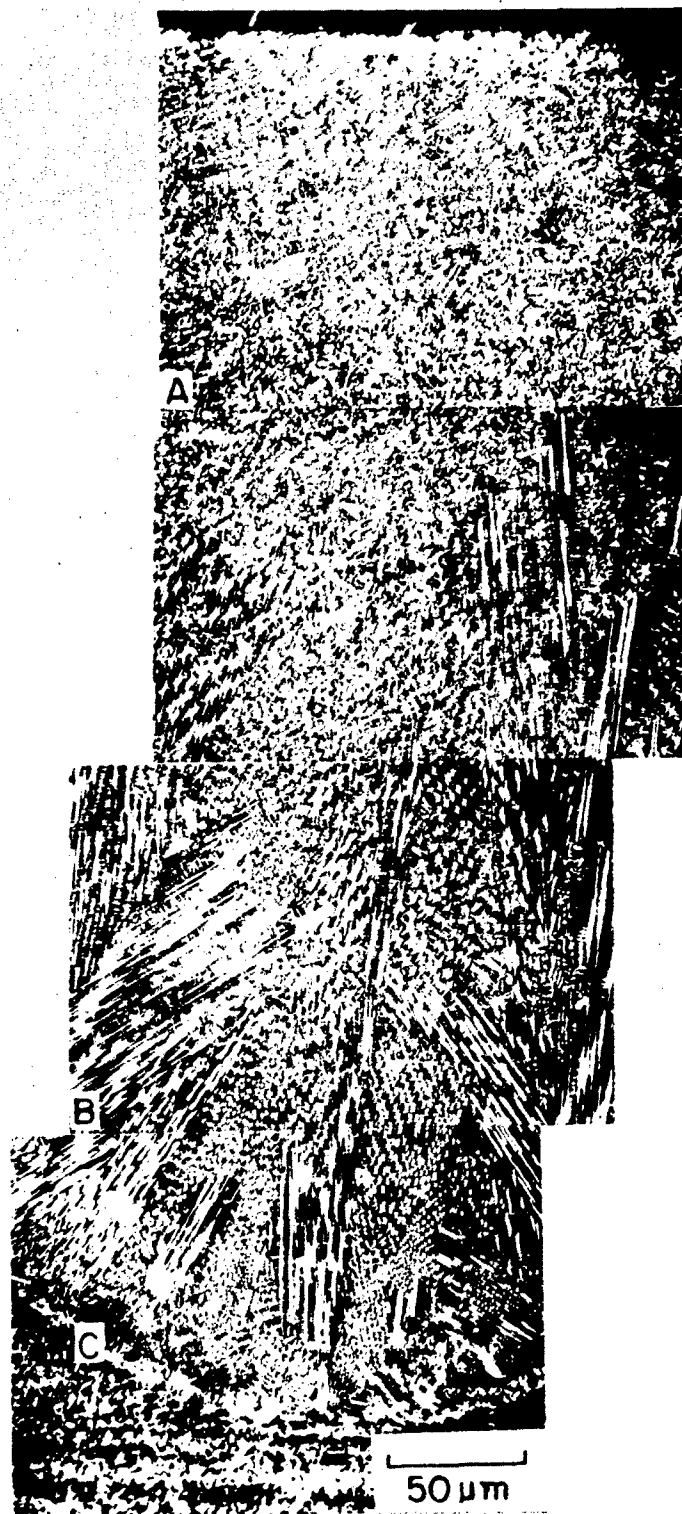


Fig. 2. Higher magnification (X450) micrograph of portion of the laser melted zone indicated in Fig. 1(b).

into the overall distribution of the δ and γ phases may be gained by etching with solutions which selectively etch each phase. Figs. 1a and b are approximately complementary in tone with the dark δ -regions in Fig. 1a revealed by Vilella's reagent and the dark γ -regions in Fig. 1b revealed with Murakami's reagent.

Microhardness measurements were made on as laser melted material and values ranged from 650 V.H.N. in the upper δ -rich region to 950 V.H.N. in the region near the maximum melt depth.

3.2 Subsequent Heat Treatment

One thermal treatment following laser melting was ageing for two hours at 560°C, this temperature is that used for tempering in conventional heat treatment. The treatment resulted in appreciable hardening in the maximum melt depth region with hardness values 1050-1100 V.H.N., see Table 2. The microstructures observed are seen in Fig. 4(a) and Fig. 6(a) using the electron microscope plastic replica and carbon extraction replica techniques respectively. In Fig. 4(a) the original cellular structure is clearly evident and in Fig. 6(a) the cell boundaries are clearly decorated with carbides (up to $\sim 0.2\mu\text{m}$). As seen in Fig. 6(a) carbide particles are also present within the cells; these appear to be more numerous in a dark field image obtained from a carbide reflection in the diffraction pattern than is apparent in Fig. 6(a). The carbide dispersion undoubtedly accounts for the high hardness.

A rather different type of microstructure is formed by austenitizing the specimen for 1 hour at 1230°C and then quenching into liquid nitrogen. As shown in Fig. 4(b) a well-defined sub-boundary structure now exists within larger size grains, the diameter of the sub-grains being comparable to that of the original cells in as laser melted material. In addition, $\sim 1\mu\text{m}$ diameter carbide particles decorate both grain boundaries and sub-boundaries. The car-

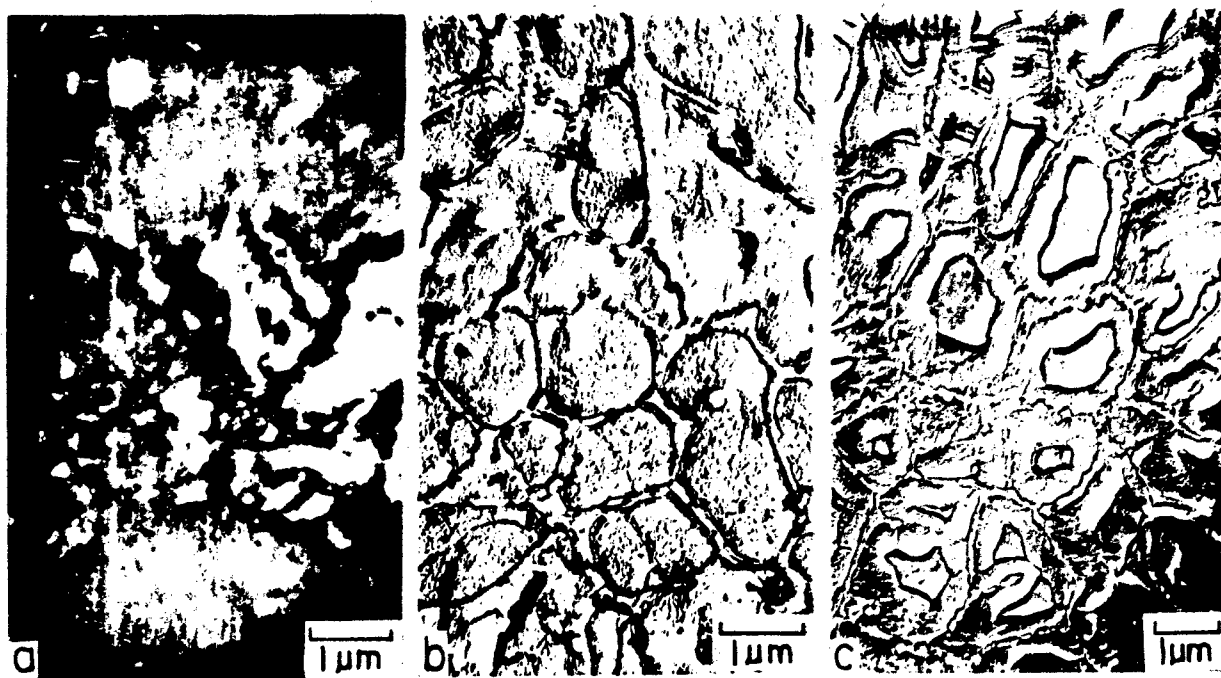


Fig. 3. Electron micrographs of as-laser melted material showing: (a) & (b) δ -ferrite cellular microstructure in the upper melt zone as revealed by a dark-field thin-film and replica micrograph; regions which have transformed to austenite are in light contrast. (c) a peritectic microstructure in the middle of the melt zone as revealed by a replica.

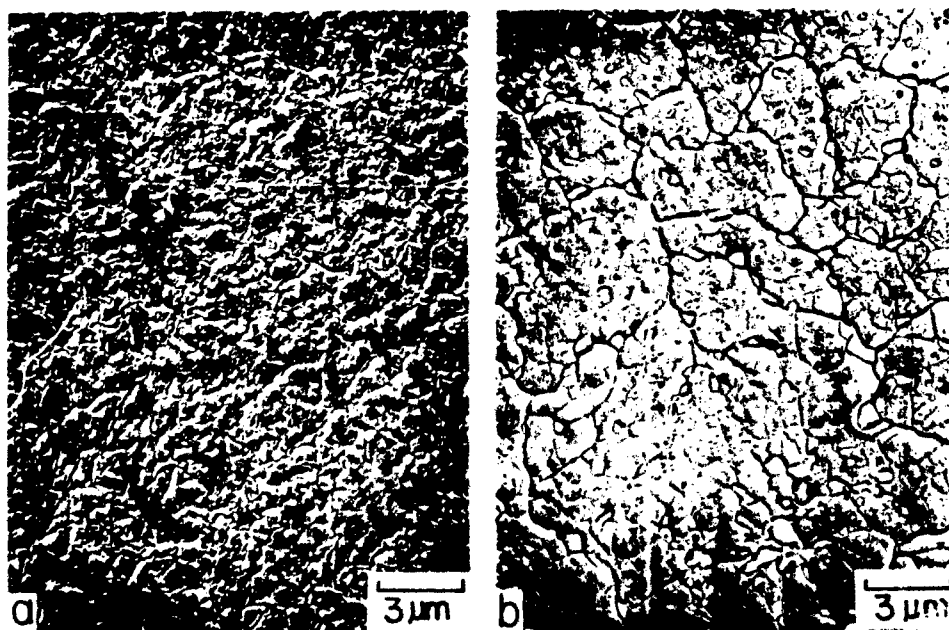


Fig. 4. Electron microscope replica micrographs of subsequently heat treated at: (a) 560°C where cellular microstructure is still clearly evident; (b) 1230°C where a well-developed sub-boundary structure has formed.

bide extraction replicas in Figs. 6(b) and (c) do not clearly reveal the sub-grain structure as in Fig. 4(b), however, another important feature is a dense distribution of both fine ($\sim 0.2 \mu\text{m}$) and extremely fine ($\sim 20 \text{nm}$) carbide particles as well as the relatively large carbides ($\sim 1 \mu\text{m}$). The extremely fine particles (Fig. 6(c) in the vicinity of grain boundaries were identified as carbides by imaging with carbide reflections in the diffraction pattern. This fine scale carbide dispersion thus accounts for the high hardness values (1030-1100 V.H.N.) which shows only a small variation throughout the melt zone, see Table 2. Finally, another very significant feature is the complete lack of microstructural evidence of martensite, this is also noted in studies on slowly directionally solidified M2 tool steel (9-11).

3.3 Carbide Crystal Structure

The crystallographic structure of carbides in both as-laser melted and subsequently heat treated material was determined from electron diffraction patterns of the extraction replicas, see Table 3. The amount of etching required for carbide extraction depended upon the nature of the matrix and in some cases it was sufficient to produce pronounced surface relief effects, as in Fig. 5(a). Regions representative of the upper and lower melt zones and heat affected zone in the as-melted condition are shown in Figs. 5(a), (b), and (c) respectively. Diffraction patterns, as in the insert in Fig. 5(a), show M_2C type carbides are in predominance throughout the entire melt region, other carbides are of the M_{23}C_6 type. In Fig. 5(a) the small M_2C type carbides are mainly concentrated within the regions between the δ -cells. Small carbide particles are also evident in the interdendritic regions in the lower melt zone in Fig. 5(b), where the matrix is entirely austenitic. The crystal structure of these carbides was not identified since attempts to extract them were unsuccessful. However, the fine particles in the heat affected zone were readily extracted, although M_2C -type carbides were present the dominant type was the M_{23}C_6 structure.

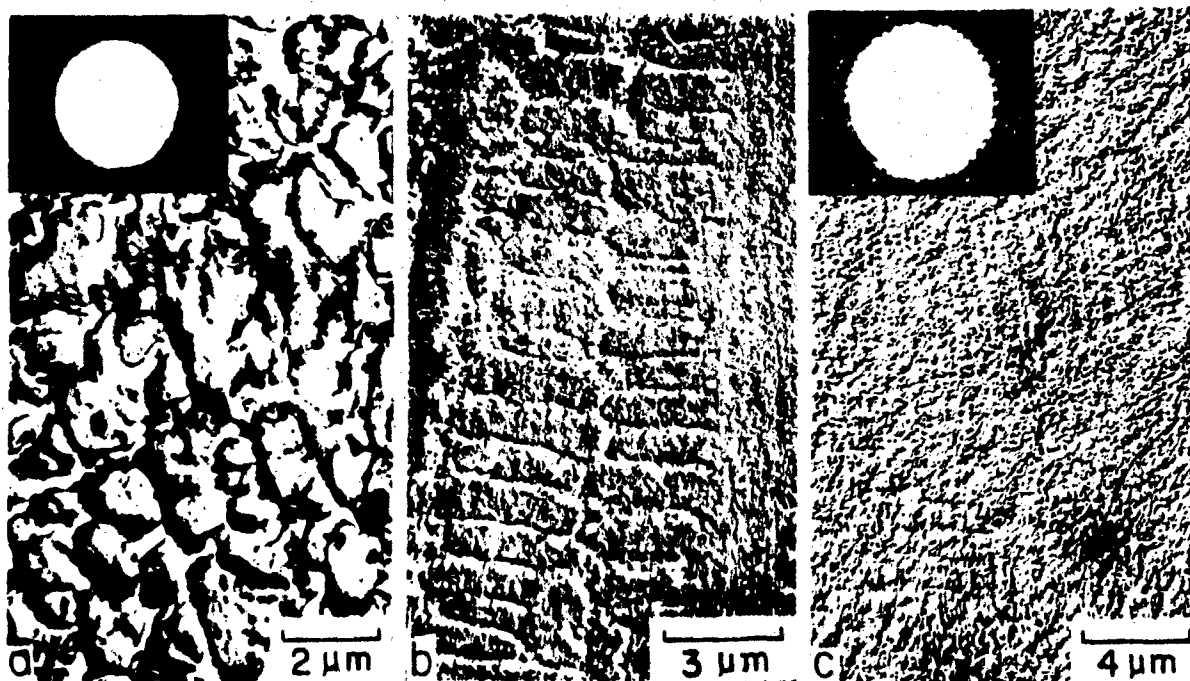


Fig. 5. Electron microscope replica micrographs showing carbides in as-laser melted material in regions in: (a) upper melt zone; (b) lower melt zone; (c) heat affected zone.

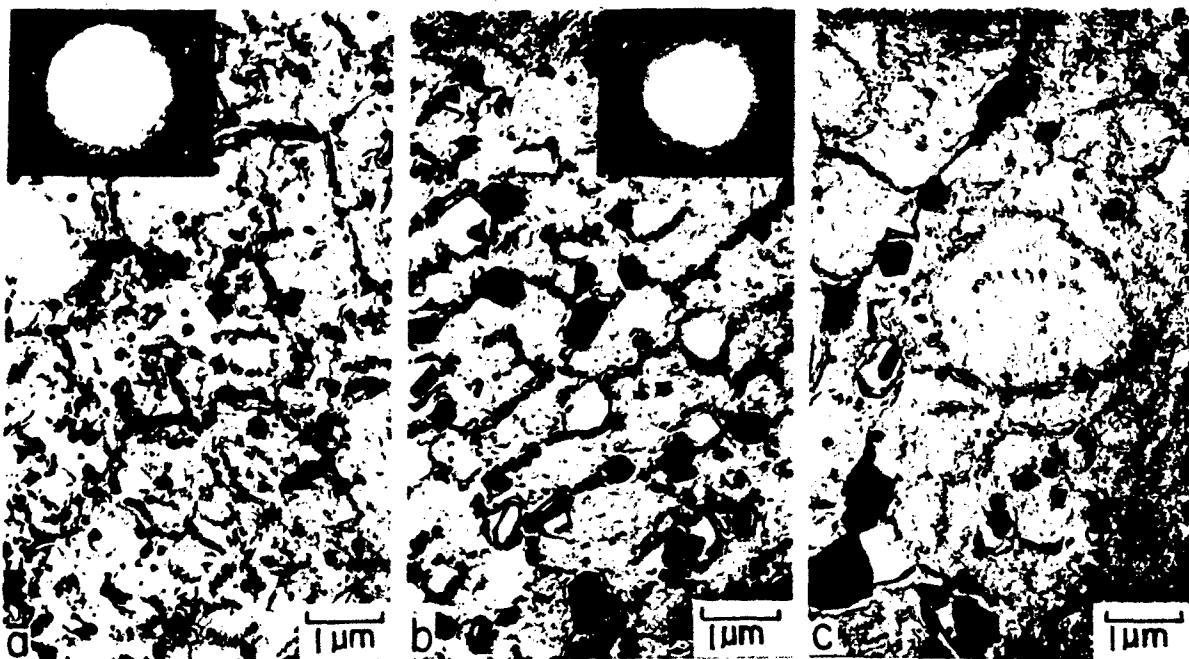


Fig. 6. Electron microscope carbide extraction replicas of material heat treated at: (a) 560°C for 7.2×10^5 s; (b) & (c) 1230°C for 300s. For details see text.

Subsequent heat treatment profoundly modifies the type, distribution, and size of carbide particles. In material tempered at 560°C, see Fig. 6(a), there are both $M_{23}C_6$ and M_2C -type carbides with $M_{23}C_6$ in predominance. However, the material annealed at 1230°C and then quenched into liquid nitrogen shows only MC_{1-x} type carbides. As seen in Figs. 6(b) and (c) this MC_{1-x} carbide phase exists as a dispersion of fine particles ($\sim 20\text{nm}$ dia.) and as large carbide particles ($\sim 1\text{ }\mu\text{m}$).

4. DISCUSSION

The present study shows that a specimen of the alloy M2 undergoing a single laser melting and cooling cycle displays similar microstructural features to one subjected to several cycles (2). Namely, a two phase δ -ferrite and austenite (γ) matrix containing a low concentration of fine carbide particles. The morphology of these phases and the extent to which the peritectic reaction proceeds depends upon the cooling rate C ($^{\circ}\text{C}.\text{s}^{-1}$), gradient G ($^{\circ}\text{C}.\text{cm}^{-1}$) and melt interface velocity R ($\text{cm}.\text{s}^{-1}$); these parameters continuously vary during solidification. Calculations (4) show that as the liquid/solid interface moves from the maximum melt depth to the surface the cooling rate C remains constant after an abrupt initial increase, whereas G decreases and R increases. A particularly striking feature of laser melting is the high value of G/R in the lower melt region. This facilitates the growth of dendrites along radial heat flow directions as is well apparent in Fig. 2. Interestingly, the mean value of G/R in a shallow laser melt zone may be sufficiently low that dendritic growth is not observed, see for example Fig. 5.

Considering the distribution of phases throughout the melt zone, it is noted that a previous study (2) has shown the matrix in the lower melt region is completely austenitic. Thus the peritectic reaction $\delta + \text{liquid} \rightarrow \gamma + \text{carbide}$ has gone to completion. The situation is different in the upper melt region since the matrix is predominantly δ -ferrite. The equiaxed structure in this

zone forms by nucleation and growth of δ -ferrite which later reacts with the carbon enriched liquid to form austenite and carbides. However, this reaction is promptly arrested since the high freezing rate severely reduces the redistribution of alloying elements by diffusion. The fact that the high volume fraction of δ -ferrite persists at room temperature for a long period of time may lead one to conclude that the outer region of the δ -ferrite cell is very high in ferrite stabilizing elements (Mo, W, Cr, V) in an agreement with McLaughlin *et al.* (9) The peritectic microstructure in Fig. 3(c) is qualitatively identical to that obtained by slow directional solidification, however, the scale is ~ 200 times smaller. The reason for this degree of microstructural refinement is the high liquid/solid interface rate ($R \sim 50 \text{ cm. s}^{-1}$) produced by laser melting. This value deduced from a heat transfer analysis (4), compares with that of $9 \times 10^{-4} \text{ cm. s}^{-1}$ obtained during slow directional solidification. The square root of the ratio of the rates gives the ratio of the diffusion distances of the redistributing alloying elements in the two solidification processes. This ratio is ~ 200 which is the scaling factor between the microstructure in *r.f.* 9 and Fig. 3(c).

The results of the present experiments strongly resemble those in splat quenching studies of tool steels (6,7) and a Fe-10% Mo-0.5%C alloy (6). Specifically, the microstructure consists of a carbide dispersion in a matrix with varying proportions of a f.c.c. phase and a b.c.c. phase with no detectable tetragonality. This study shows that a large proportion of the carbides form by peritectic reaction and an example of this is clearly seen in the intercellular region in Fig. 5(a). Obviously, carbides within the δ -ferrite must form by solid state transformation and undoubtedly some carbides within the austenite also form this way. The two surprising findings in the carbide extraction and identification experiments are the abundance of M_2C and the complete absence of M_6C carbides. The other phase found in the as-melted state is $M_{23}C_6$.

The effect of subsequent heat treatment is interesting since only MC_{1-x} carbides are present following high temperature annealing at 1230°C. In contrast, following low temperature annealing at 560°C only $M_{23}C_6$ and M_2C carbides are present, but unlike the as-laser melted state $M_{23}C_6$ is the dominant carbide. The striking difference in conventionally heat treated material is that a significant proportion of the carbides are of the M_6C type whereas only a low proportion are of the M_2C type.

The microstructural variation of as-laser melted material contrasts strongly with the homogeneity of material given subsequent heat treatment at 1230°C. This is reflected by the microhardness measurements in Table 2. In the as-laser melted state the δ -ferrite rich region in the upper melt zone is relatively soft (650 V.H.N.) whereas the austenitic lower region is hard (950 V.H.N.). Presumably solid solution strengthening by a high carbon concentration accounts for the high strength of the austenite since there is no evidence of a higher preponderance of carbides in the lower melt region.

The uniformity of high microhardness values throughout the entire melt region following heat treatment at 1230°C is particularly interesting. Obviously, the homogeneous carbide dispersion giving rise to this involves a redistribution of carbon atoms over appreciable distances. The mean diffusion distance involved is found by assuming the usual diffusion parameters (11) for the diffusion of carbon in ferrite. For a time of 7.2×10^3 s at 560°C this is $\sim 300\mu m$ which is nearly identical to that for the diffusion of carbon in austenite at 1230°C for the time of 3×10^2 s. As is readily appreciated in Fig. 1 the mean diffusion distance is sufficient for a redistribution of carbon atoms necessary to produce a homogeneous carbide dispersion.

Finally, an interesting feature of the heat treated material is the small cell or sub-grain size ($\sim 1.5\mu m$). It is thus tempting to anticipate that the combined effect of a fine carbide dispersion and a small cell size will contribute to good ductility and thus an increased toughness of tool steels hardened by the techniques just discussed.

5. Acknowledgement

The authors wish to acknowledge the support of this investigation by the Office of Naval Research, contract number N00014-78-C-0580.

References

1. E.M. Breinan, B.H. Kear, C.M. Banas, and L.E. Greenwald, "Superalloys: Metallurgy and Manufacture", p. 435, 3rd International Symposium, Seven Spring, PA 1975.
2. P.R. Strutt, M. Tuli, H. Nowotny, and B.H. Kear, *Materials Sci. and Eng.*, 1978, vol. 36, p. 217.
3. M. Tuli, P.R. Strutt, and B.H. Kear, Conference of Rapidly Solidification Processing, Reston, Virginia, Dec., 1977.
4. M. Tuli, Master Thesis at the University of Connecticut, 1977.
5. L.E. Greenwald, Report R77-111321-1, United Technologies Research Center, East Hartford, Connecticut, 1977.
6. H. Matyja, B.C. Giessen, and H.J. Grant, *J. Inst. Metals*, 1968, vol. 9, p. 30.
7. I.R. Sare and R.W.K. Honeycome, 2nd Int. Conference on Rapidly Quenched Metals, ed. H.J. Grant and B.C. Giessen, M.I.T. Press, 1976.
8. J.J. Rayment and B. Cantor, *Met. Sci.*, 1978, vol. 12, p. 156.
9. H. Fredriksson, *Met. Sci.*, 1976, vol. 3, p. 77.
10. J. McLaughlin, R.W. Kraft, and J.I. Goldstein, *Met. Trans.*, 1977, vol. 8A, p. 1787.
11. R.H. Barkalow, R.W. Kraft, and J.I. Goldstein, *Met. Trans.*, 1972, vol. 3, p. 919.
12. C.J. Smithells, *Metals Reference Book*, 1967, vol. 2, p. 556.

Table I. Average Composition of M2 Steel

<u>Elements</u>	<u>M2 Steel</u>	
	<u>Wt. %</u>	<u>At. %</u>
C	0.85	4.06
Mn	0.25	0.26
Si	0.30	0.61
P	0.03	0.06
S	0.03	0.05
Cr	4.2	4.63
V	1.9	2.14
Mo	5.0	2.99
W	6.35	1.98

Table II. Values of the Vickers Microhardness Number
(V.H.N.) at 100g

<u>Condition</u>	<u>Top Surface</u>	<u>Central Region</u>	<u>Maximum Meit Depth Region</u>
As-laser melted	650-700	770-900	930-950
560°C heat treatment	850-880	910-980	1050-1100
1230°C heat treatment	1020-1060	1060-1100	1060-1100

Table III. Species of Carbide in M2 Steel
Identified After Various Thermal Treatments

Treatments	Carbides	Lattice Parameters	Remarks
Annealed	M_6C , M_2C , $M_{23}C_6$		
Conventionally hardened	M_6C , M_2C		
As-laser melted	M_2C	$a = 2.8_7^{\circ}\text{\AA}$ $c = 4.5_8^{\circ}\text{\AA}$	Major carbide in δ -ferrite region. Minor carbide in heat affected region. $M=(V,Mo,W)$ or (Mo,W,V,Cr,Fe)
	$M_{23}C_6$	$a = 10.7_6^{\circ}\text{\AA}$	Minor carbide in δ -ferrite region. Major carbide in heat affected region. $M=(Cr,Mo,W)$ or (Cr,Mo,W,Fe)
Laser + 560°C	M_2C	$a = 2.8_3^{\circ}\text{\AA}$ $c = 4.5_6^{\circ}\text{\AA}$	Throughout the melt region $M(V,Mo,W)$ or as above.
	$M_{23}C_6$	$a = 10.6_5^{\circ}\text{\AA}$	Throughout the melt region $M=(V,Mo,W)$ or as above.
Laser + 1230 °C + liquid nitrogen quench	MC_{1-x}	$a = 4.2_4^{\circ}\text{\AA}$	Throughout the melt region $(V,Mo,W)C_{0.8}$

Figure Captions

- Figure 1 Cross-section of deep laser-melted region as etched with:
(a) Vilella's reagent to reveal δ -regions (dark tone)
(b) Murakami's reagent to reveal austenite (dark tone)
- Figure 2 Higher magnification (X450) micrograph of portion of the laser melted zone indicated in Fig. 1(b).
- Figure 3 Electron micrographs of as-laser melted material showing:
(a) & (b) δ -ferrite cellular microstructure in the upper melt zone as revealed by a dark-field thin-film and replica micrograph; regions which have transformed to austenite are in light contrast.
(c) a peritectic microstructure in the middle of the melt zone as revealed by a replica.
- Figure 4 Electron microscope replica micrographs of subsequently heat treated at:
(a) 560°C where cellular microstructure is still clearly evident
(b) 1230°C where a well-developed sub-boundary structure has formed
- Figure 5 Electron microscope replica micrographs showing carbides in as-laser melted material in regions in:
(a) upper melt zone
(b) lower melt zone
(c) heat affected zone

Figure 6 Electron microscope carbide extraction replicas of material
heat treated at:

(a) 560°C for 7.2×10^3 s

(b) & (c) 1230°C for 300s

For details see text.

COMPARATIVE STUDY OF ELECTRON BEAM AND

LASER MELTING OF M2 TOOL STEEL

P. R. Strutt, D. Gilbert, and M. Kurup

Department of Metallurgy, University of Connecticut,
Storrs, Connecticut 06268

Summary

To directly compare the electron beam and laser melting surface techniques a study has been undertaken to surface melt M2 tool steel by electron beam irradiation. This material was selected since the effect of laser beam irradiation melting of M2 is well characterized. Irradiation was conducted in vacuum and the highly efficient ($\approx 90\%$) and stable coupling between beam and material produced a melt zone of fairly constant depth and good surface smoothness. To simulate the laser melting conditions a 0.5mm diameter beam scanned the surface at velocities in the range 12.5 to 50 cm.s^{-1} , however the requisite beam power was 375 watts as compared with 3 to 5 kW for laser melting. For a solidification rate of $\approx 5 \times 10^{50} \text{C.s}^{-1}$, the melted zone contains regions of δ -ferrite and fine scale martensite. Following subsequent austenizing and tempering a uniform hardness of 1050 to 1150 V.H.N. is obtained throughout the entire melt region. This compares with 850 V.H.N. in conventionally treated material. Another interesting feature is that moderately refined microstructures (with cooling rates of $\approx 10^{40} \text{C.s}^{-1}$) of 950 V.H.N. are obtained at higher power densities in the deep penetration mode.

Introduction

There is considerable current interest in the use of high energy beams for producing a rapidly quenched surface layer on a metal substrate. This is the basis of the "laser-glazing" technique in which a continuous CO₂ laser beam rapidly scans a material surface so that it undergoes momentary melting followed by rapid solidification (1). The actual solidification rate depends upon power density and the relative velocity of the beam relative to the material and is in the range 10^5 to 10^8 °C.s⁻¹. Such high rates result in ultra microstructural refinement, extension of solubility limits and dissolution of high melting point carbide phases. As a result of the latter it is now possible to control both the size and distribution of carbides in a tool steel (2,3) and a hard iron-carbide composite material (4). On the basis of these intriguing discoveries it is thus of considerable technological importance to examine the possible use of electron beam surface melting for achieving comparable results.

Since electron beam technology is well-established the requisite equipment is readily available for surface melting processing. Thus, it is now important to establish the appropriate experimental conditions and determine the effect of the process parameters. This paper briefly summarizes a basic electron beam surface melting study on M2 tool steel; this alloy was selected in view of a previous study of laser surface melted material (2,3).

Experimental Method

In order to compare electron beam and laser surface melting the beam diameter (0.5 mm) and range of beam velocities (1.5 to 100 cm.s⁻¹) were the same as in the previous study of laser melted M2 tool steel (2,3). Due to a highly efficient beam/specimen energy coupling the incident beam power was adjusted to 375 watts in order to obtain a maximum melt depth comparable to that obtained with a 3kW incident power continuous CO₂ laser beam. After surface melting, the as-melted surfaces were examined in a scanning electron microscope. In addition, surface melted specimens were cross-sectioned and then observed by optical microscopy, scanning electron microscopy and the electron microscope replica technique.

Results

Surface Studies

The "ripple" structure, see Fig. 1, was observed at all beam velocities rather than within a specific range as noted by Anthony and Cline (5). The progressive change of surface morphology with increasing velocity is seen in Fig. 1, where two distinct "ripple" periodicities are evident. The mean spacing of the large amplitude ripples is from 100 μ m to 300 μ m whereas that between the fine ripples (clearly evident in Fig. 1b) is ~ 10 μ m. Recently Anthony and Cline (5) and Copley et al (6) have studied this phenomenon and it is suggested (6) that the coarse ripples are

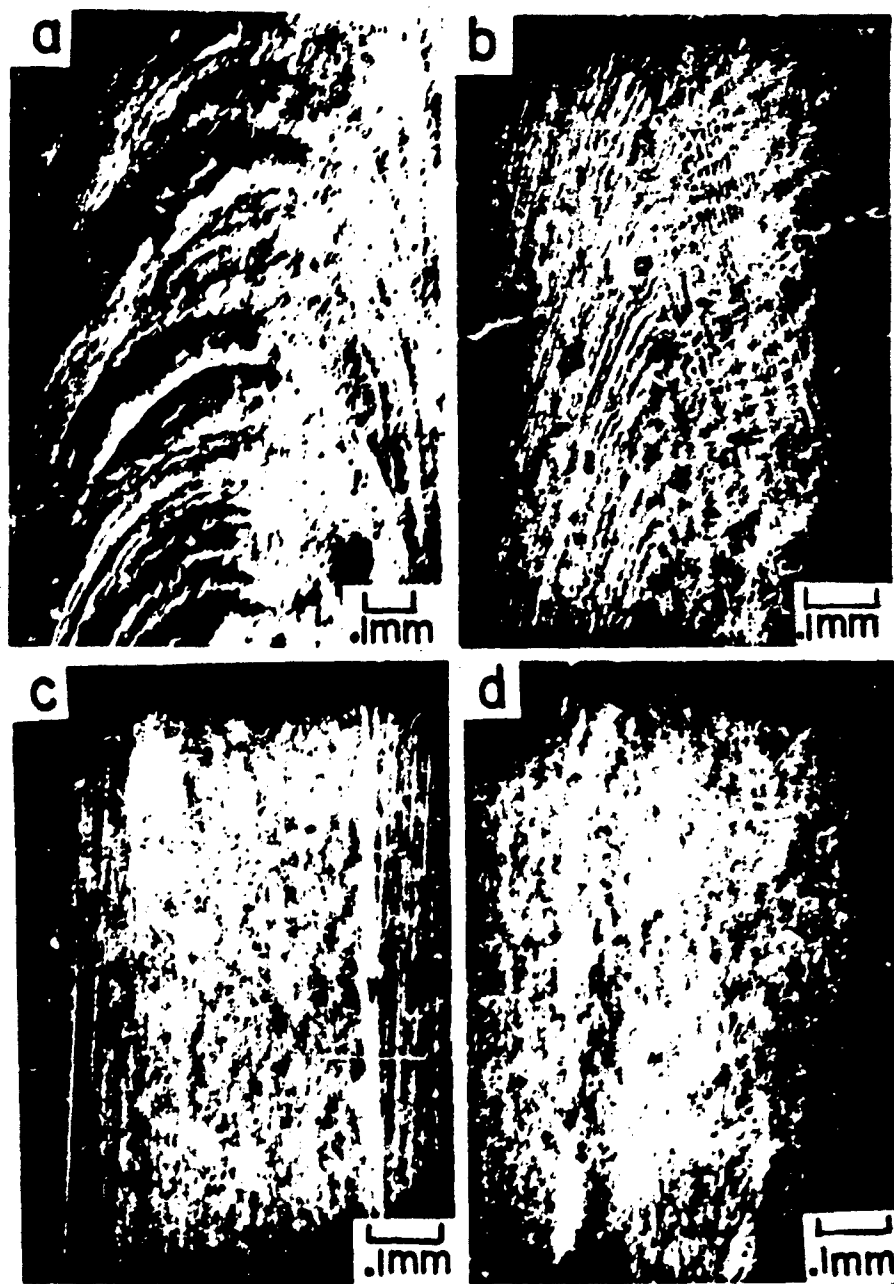


Fig. 1. Scanning electron micrographs of surface ripple structure for beam velocity of (a) 1.7 cm.s^{-1} , (b) 4.25 cm.s^{-1} , (c) 57.5 cm.s^{-1} , and (d) 97.50 cm.s^{-1} .

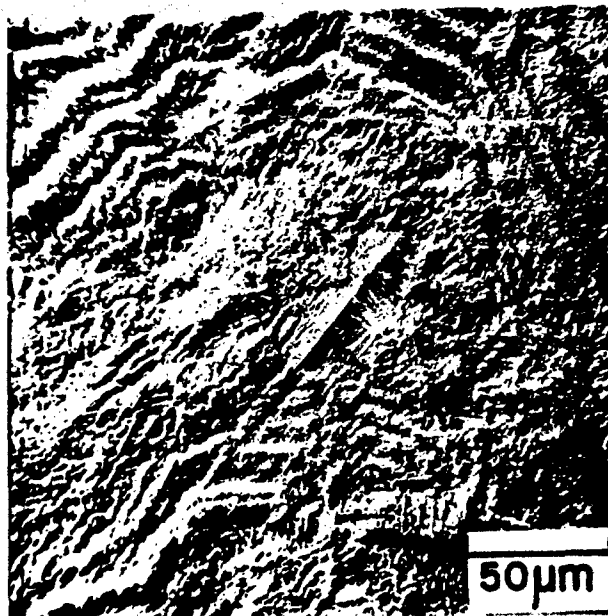


Fig. 2. Scanning electron micrograph of as-melted structure showing "segmented" fine scale ripples and surface dendrites; beam velocity is 4.25 cm.s^{-1}

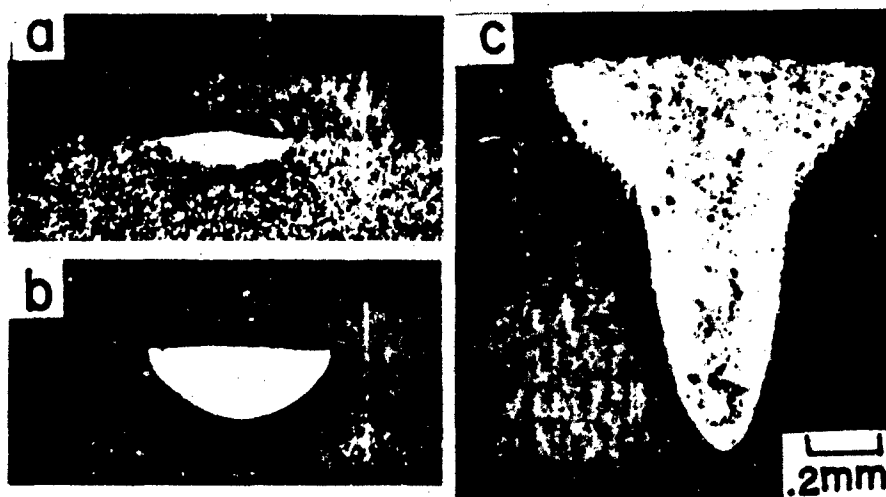


Fig. 3. Cross-sectional micrographs showing effect of interaction time on size and shape of melt zone. The interaction times are (a) $1.3 \times 10^{-3} \text{ s.}$, (b) $6 \times 10^{-3} \text{ s.}$ and (c) $1.2 \times 10^{-2} \text{ s.}$

created by a periodic overflow of liquid at the trailing edge of the molten pool. The fine ripples presumably result by the freezing in of surface waves and their absence at higher velocities may well arise from the attenuation in the shallow molten pool.

An unusual feature noted at beam velocities of 4.0 and 8.5 cm.s⁻¹, is the highly serrated nature of the fine solidification ripples with the segments aligned along specific directions, see Fig. 1b. This intriguing effect, not previously reported, suggests that the solidification surface is stabilized by becoming faceted (on a macroscopic scale) on specific crystallographic planes.

Melt Zone Geometry

The cross-sectional views in Fig. 3 show the strong dependence of melt zone geometry on the beam/material interaction time; this is defined as the ratio of beam diameter to the velocity. In Fig. 4 the maximum melt depth and width are shown as a function of interaction time and three distinct regions are evident. At short interaction times (region 1) the melt depth is a fraction of the width as shown in Fig. 3a where τ (interaction time) is $< 1.3 \times 10^{-3}$ s. In this regime the heat flow will be essentially inward (normal to the surface) as in the semi-infinite model of Greenwald et al. (7). At higher values of τ (region 2) the melt depth only increases slowly with τ although the depth becomes $\sim 1/3$ the width when τ is 6×10^{-3} s., i.e., near the termination of region 2. With this melt zone geometry, see Fig. 3b, the heat flow is now essentially radially outwards. When τ increases further ($> 1.2 \times 10^{-2}$ s.) surface vaporization becomes appreciable and in Fig. 3c ($\tau = 3.1 \times 10^{-2}$ s.) the beam has clearly penetrated as in the "deep penetration" mode to produce a maximum melt depth of ~ 1200 μ m.

In considering the effect of τ on melt zone width, one important factor is the actual nature of the energy distribution in the beam. Since, in most cases, this is Gaussian, the width of the irradiated zone at the surface momentarily raised to $T > T_m$ will decrease with decreasing values of τ ; T_m is the melting point temperature. This effect is readily apparent in Fig. 4, where, in fact, the melt zone width is less than the measured beam diameter (~ 0.5 μ m) when $\tau > 4.0 \times 10^{-3}$ s. Another factor determining the melt width is the temperature increase arising from lateral heat flow, i.e., in the direction orthogonal to the beam axis and the direction of beam motion. This is clearly a very important factor when $\tau > 4.0 \times 10^{-3}$ s., see Fig. 4, and in fact increasing τ from 4.0×10^{-3} to 5.0×10^{-3} s. causes $\sim 35\%$ increase in maximum width.

Various heat flow models have been proposed (7-10) for calculating the temperature distribution both for surface melting conditions ($T < T_v$) and the deep penetration ($T > T_v$); T_v is the vaporization temperature. A simple model is that of Greenwald et al (7) who envisaged a semi-infinite plate whose surface receives incident power for an interaction time τ . In the present

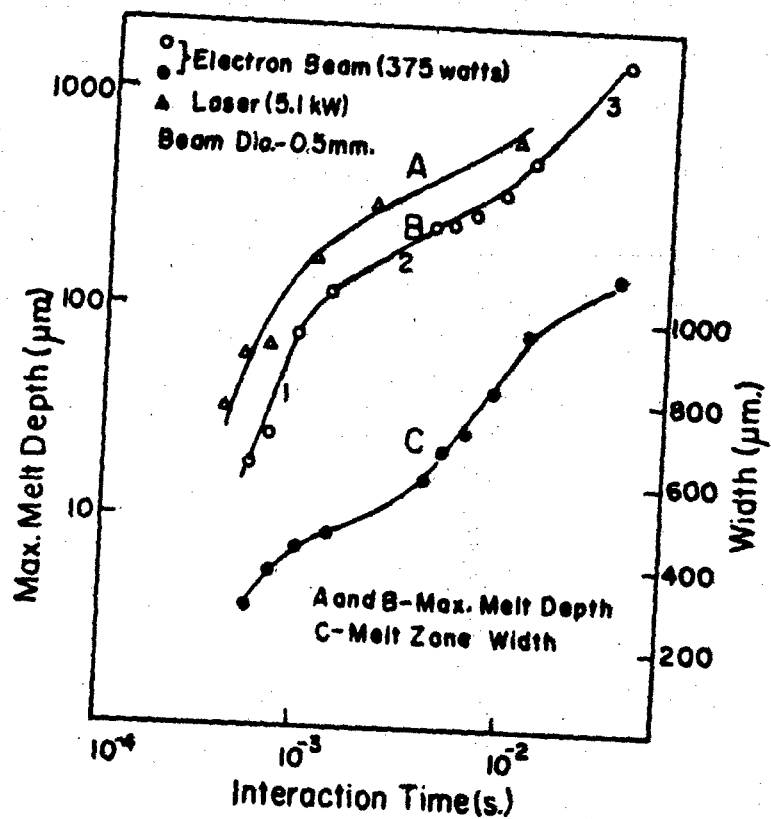


Fig. 4. The effect of interaction time on melt depth and width produced by a 375 watt electron beam. Included, for comparison, is the melt depth curve produced by a 5.1 kW laser; in each case the beam diameter is 0.51 mm.

situation a continuously moving incident beam is assumed to have a value of τ given by (beam diameter)/(beam velocity). The analysis is conveniently rearranged by introducing the parameters a and b , see equation 1.

$$a = \sqrt{4\alpha/\pi} ; \quad b = q_0/\kappa \quad (1)$$

where α and κ are the thermal diffusivity and thermal conductivity which are taken as $0.22 \text{ cm}^2.\text{s}^{-1}$ and $0.76 \text{ joule. cm.}^{-1}.\text{s.}^{-1}.\text{K}^{-1}$; the difference between the melting point and ambient temperature ($T_m - T_0$) is taken as 1390°K . From measurements of the maximum melt depth and length of the trailing liquid zone (L) the absorbed power is determined to be $\sim 125,000 \text{ watt.cm.}^{-2}$. The value of L is $V(\tau' - c)$, where c and τ' are the time for initial melting and final solidification at a point on the surface from the moment the power is applied. It may be shown that

$$c^{1/2} = (T_m - T_0)/ab; \quad (2a)$$

$$\tau' = (\tau + c)^2/4c; \quad (2b)$$

Table II compares observed (ii) and calculated (i) values of L in the higher velocity range where the semi-infinite model is a reasonable assumption.

Finally, using the same model (7) computer determined values of the maximum melt depth D are compared with experimental values obtained from cross-sectional micrographs, see Table II. On the basis of this comparison between prediction and observation the energy coupling between beam and material is $\sim 65\%$ efficient.

Cooling Rate

From the same model (7) it may be shown that the solidification rate \dot{T} is given by equation 3

$$\dot{T} = -2abc^{3/2}/(\tau^2 - c^2) \quad (3)$$

Values of \dot{T} calculated from this equation are shown in Table II and compared with empirical values determined from mean cell diameter (λ) measurements. Actual values of λ , given in Table I, are for six surface melted samples each scanned with a different beam velocity (V). The adjacent column lists the corresponding values of \dot{T} as calculated from the empirical relation $\dot{T} = (4.57 \times 10^{-8}) \lambda^{-n}$ of Matyja, Giessen, and Grant (11), where $1/n \sim 0.32$. From these values an empirical relation (equation 4) was obtained with a correlation coefficient of 0.991.

$$\dot{T} = (2.07 \times 10^4) V^{1.20} \quad (4)$$

The comparison of empirical and calculated values of \dot{T} in Table II is for the regime where the model of Greenwald et al (7) is reasonably valid; i.e., region 1 in Fig. 4. The agreement is fairly good since, on average, the empirical and calculated values of \dot{T} differ by a factor of 2.

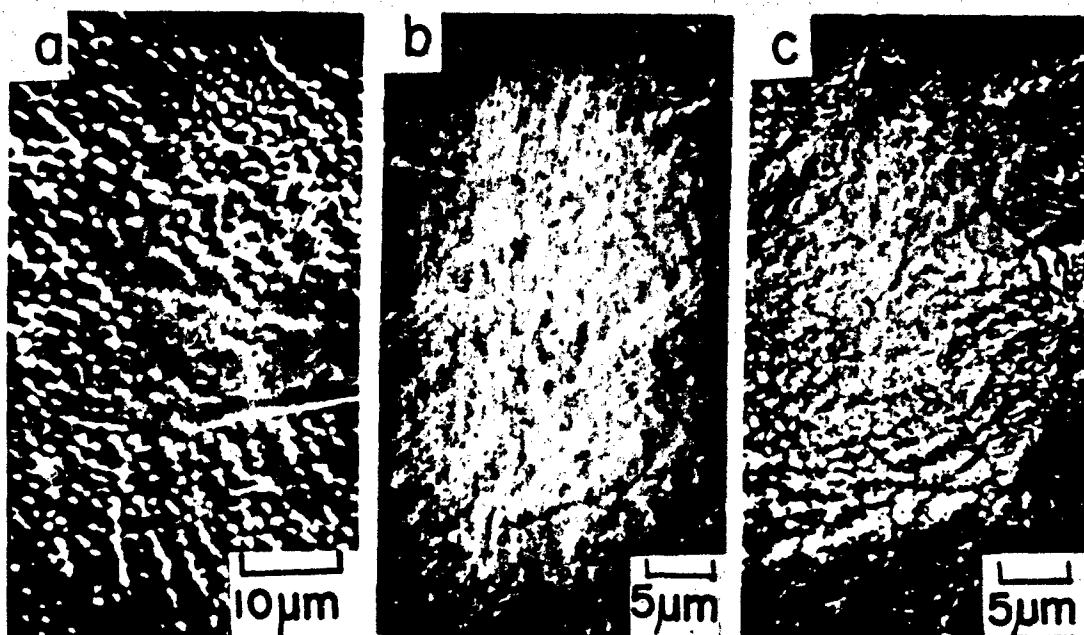


Fig. 5. Scanning electron micrographs showing increasing refinement of cellular/dendrite structure in as-melted surface with increasing beam velocities. Beam velocity is (a) 1.7 cm.s^{-1} , (b) 38 cm.s^{-1} , (c) 76 cm.s^{-1} .

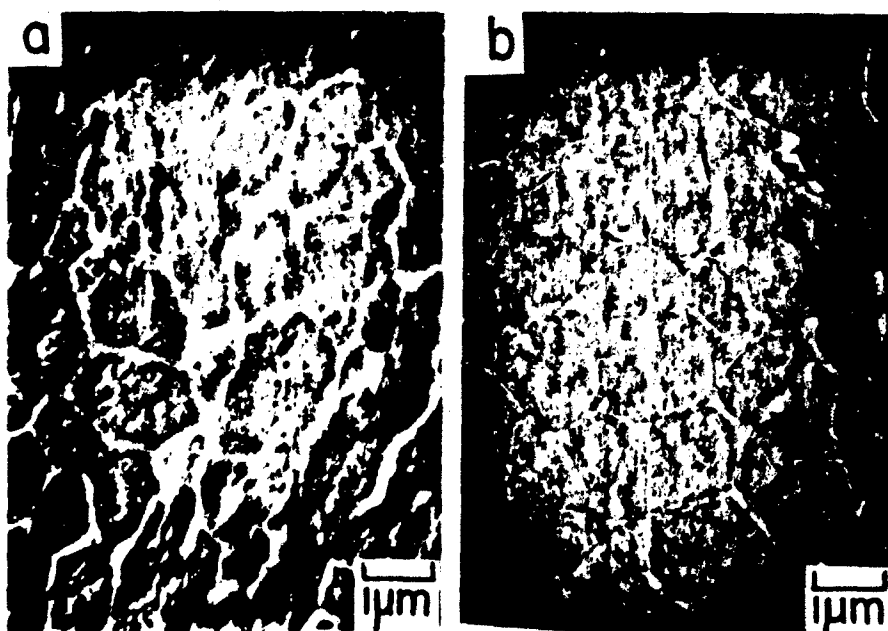


Fig. 6. Cellular δ -ferrite obtained by (a) electron beam and (b) laser melting and revealed by (a) scanning and (b) replica transmission microscopy.

Microstructural Observations

The nature and scale of the surface microstructure depends upon beam velocity (interaction time) and in most cases varies across the surface from center to edge. At the lowest beam velocity (1.7 cm.s^{-1}) an equiaxed cellular structure is observed throughout the entire surface area, see Fig. 5a. It is interesting to note that a similar microstructure was seen near the surface in metallographic sections made from laser melted material (2,3). Beam velocity markedly affects the surface morphology and when $v > 1.7 \text{ cm.s}^{-1}$ surface dendrites appear and become more and more refined and extensive as v is increased, see Fig. 5b, where $v = 38 \text{ cm.s}^{-1}$. A rather curious microstructural feature is the fine scale "surface crazing" which occurs in melting at the higher beam velocities, see Fig. 5c. This apparently results from an insufficient amount of liquid to solidify in the interdendritic regions at the center of the melt zone.

The present comparative study shows an equivalence of the electron beam and laser in producing a highly refined microstructure in M2 tool steel. This is based on observations of the melted zone below the surface. On the actual as-melted surface the laser does not produce a morphological condition of sufficient quality for detailed microstructural observation. In sectioned metallographic samples, however, a direct comparison may be made between electron beam and laser surface melting. The similar cellular microstructure near to the surface in (a) an electron beam and (b) a laser melted specimen is readily apparent in Fig. 6. The scanning micrograph in Fig. 6a is of a subsequently heat treated sample whereas the replica micrographic in Fig. 6b is of a sample in the as-melted condition. The heat treatment of the specimen in Fig. 6a consisted of heating at 560°C for $3.6 \times 10^3 \text{ s}$ followed by oil quenching. This produced the discernible fine bainitic/ or martensitic structure; it should be noted that this results after heat treatment of either electron beam or laser melted specimens. The attainable hardness as a result of this treatment is from 950 to 1050 V.H.N., as compared with a value of 800 V.H.N. in conventionally hardened material.

Another heat treatment was heating at 1230°C for 300 s. followed by a quench into ice-brine, this results in precipitation of small MC_{1-x} carbides as is evident in Fig. 7. The carbide distribution is equally well revealed in the scanning electron micrograph (Fig. 7a) and the replica micrograph (Fig. 7b). It is interesting that the fine martensitic structure is revealed in the scanning electron micrographs and the fine sub-boundary structure in the etched and subsequently replicated sample. The microhardness produced by this heat treatment is from 1000-1050 V.H.N., irrespective of whether the initial rapid solidification was by electron beam or laser.

The salient finding in the present investigation is the equivalence of electron beam and laser surface melting in producing a highly refined microstructure in M2 tool steel which can subsequently be hardened to an extent manually unattainable. The difference, however, is the significantly higher beam/material

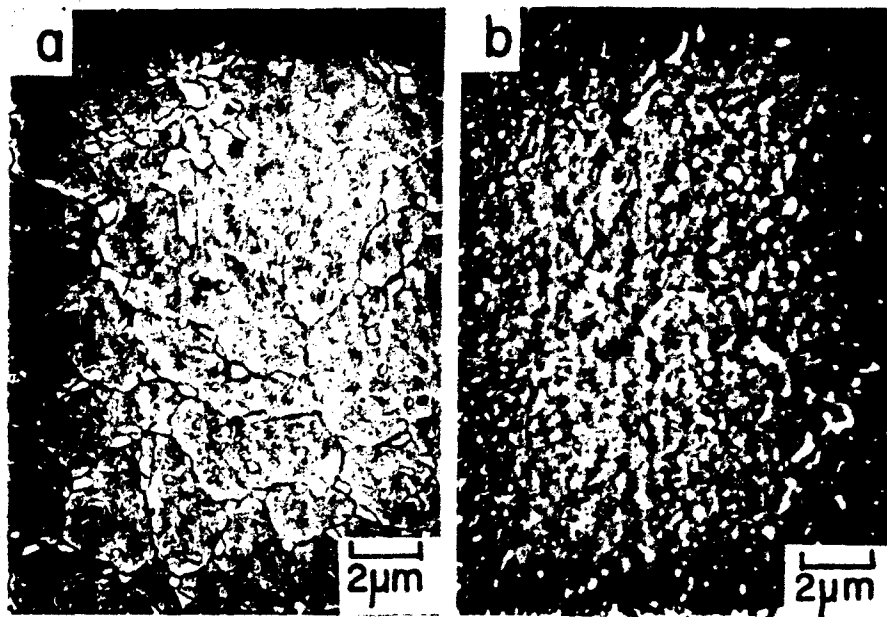


Fig. 7. Carbide dispersion in M2 tool-steel subsequently hardened by heating at 1230°C for 300 s. and quenching into liquid nitrogen; these microstructures are revealed by (a) scanning and (b) replica transmission microscopy.

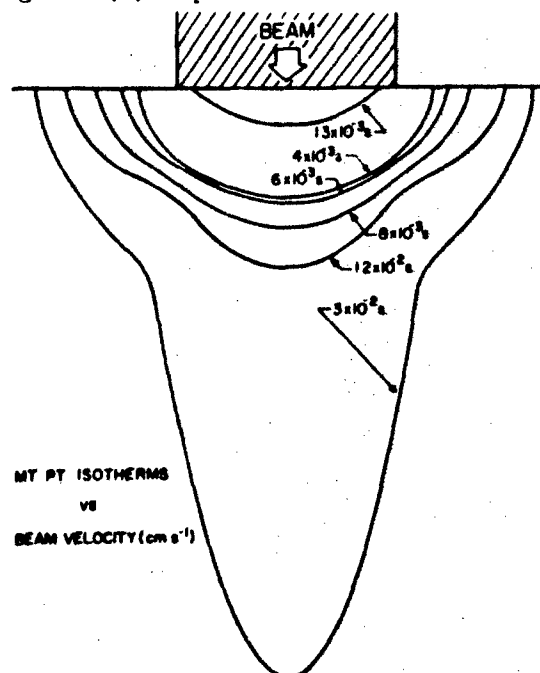


Fig. 8. Maximum extent of melting point isotherm as a function of beam/substrate interaction time (obtained from actual cross-sectional micrographs).

energy coupling achieved by electron beam surface melting. This is clearly apparent in Fig. 4, where a 5.1 kW laser beam does not produce a vastly greater depth of melting than a 375 watt electron beam of the same spot diameter (~ 0.5 mm). Finally, another attractive feature of electron beam surface melting is the exceeding good metallurgical condition of the as-melted surface.

Heat and Fluid Flow Mechanisms and Their Effect on Melt Zone Geometry

We now consider further aspects of the rapid solidification mechanisms and the changes involved when processing parameters are varied. The effect of changing the beam/substrate velocity for constant beam power is shown in Fig. 4. Region 1 corresponds to the type of surface melting discussed by Greenwald et al (7) where the maximum temperature T is in the range $T_v > T > T_m$, where T_v and T_m are the vaporization and melting temperature. Defining V_v and V_m as the beam velocities corresponding to maximum surface temperatures T_v and T_m the analysis in ref. 7 shows that the ratio V_v/V_m is given by equation 5.

$$V_v/V_m = (T_m - T_o)^2 / (T_v - T_o)^2 \quad (5)$$

For the present alloy V_v/V_m is ~ 3 since V_m is something in excess of 100 cm.s^{-1} . The minimum beam velocity before the onset of surface vaporization is $\sim 30 \text{ cm.s}^{-1}$. Below this value the beam penetrates into the material and if the penetration is sufficient a plasma cavity is formed.

In region 2 (Fig. 4) the melt depth and width increase with increasing interaction time (τ) over the range $6 \times 10^{-3} \text{ s} > \tau > 1.5 \times 10^{-3} \text{ s}$. Actual melting temperature isotherms corresponding to specimens irradiated at different beam velocities are shown in the profiles obtained from cross-sectional micrographs in Fig. 8. Within region 2 (Fig. 4) the shape of the melt zone would suggest melting by simple radial heat flow from the incident beam into the semi-infinite substrate; i.e., there is no slight protruberance that one might expect by "keyholing". This, however, is not entirely correct since, as already shown, the values of τ exceed that for surface vaporization. Furthermore, in the actual melting experiments a plasma cavity was observed when $\tau > 4 \times 10^{-3} \text{ s}$. Another point of interest is the negligible change in melt depth when τ is increased from 4×10^{-3} to $6 \times 10^{-3} \text{ s}$ as contrasted with the significant increase when τ is increased by a corresponding amount (50%) from $8 \times 10^{-3} \text{ s}$ to $1.2 \times 10^{-2} \text{ s}$. As revealed by the protruberance on the melting temperature isotherm this is indicative of deep beam penetration into the liquid. When the interaction time τ is further increased the beam penetrates the material to an even greater extent. The melting isotherm for $\tau = 3 \times 10^{-2} \text{ s}$ clearly shows the onset of the "deep penetration mode" which will be further discussed.

As already discussed several workers have considered moving point source and line source heat flow models (8-10). The pertinent hydrodynamics involved, however, has received less attention and consequently we now consider this highly important aspect.

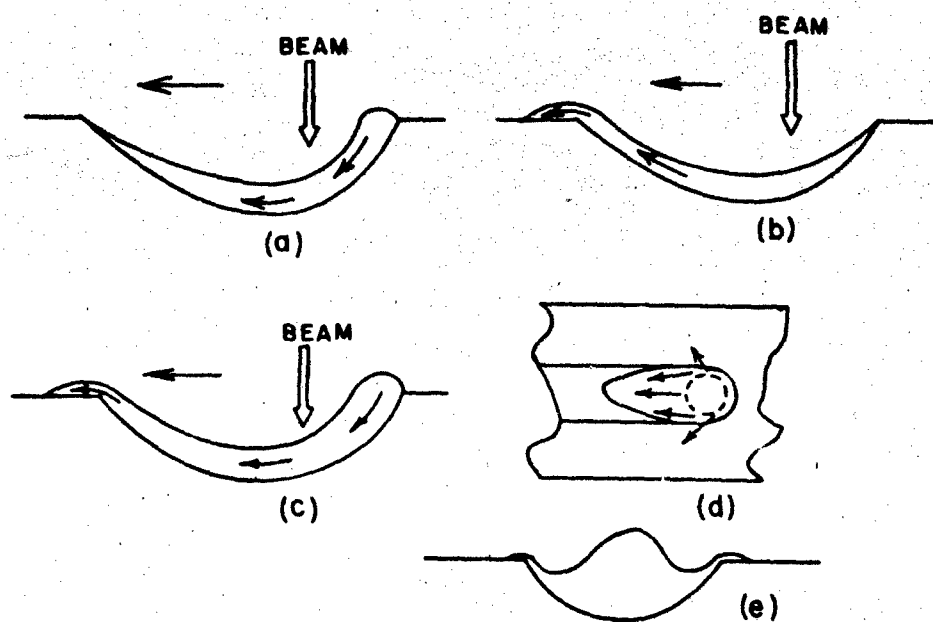


Fig. 9 Schematic diagram showing the formation of the depression beneath the beam and liquid flow to form (a,b) surface ripples (c-e) a continuous central ridge and side troughs.



Fig. 10 Cross-sectional micrographs showing the effects of increased beam power in forming side troughs and a central ridge. The beam velocity is 55.7 cm.s^{-1} and the power for (a) and (b) are 550 and 750 watts respectively.

Some fluid mechanics considerations giving rise to high amplitude-low frequency ripples and the central ridge-side trough topography (see Fig. 9e) are summarized in Fig. 9. This both combines and extends previous concepts and observations (6,12). The critical feature, leading to all subsequently phenomena, is the depression beneath the incident beam, contributory causes of this are (i) the progressive increase in surface tension between the center and edge of the molten pool (5), (ii) the "keyhole" due to actual beam penetration into the material. Motion of the material, relative to the beam, results in formation of a liquid bulge ahead of the beam, which as shown in Fig. 9a, causes liquid flow beneath the beam. This, then, results in liquid overflow at the trailing edge as shown in Fig. 9b. The formation rate of liquid in the bulge ahead of the beam is determined by the velocity and beam power density. For instance, with a low power incident beam it will take awhile before a sufficient liquid bulge forms for liquid flow to the trailing edge to occur. Overflow at the trailing edge will thus be periodic and result in ripple formation. However, with a high power incident beam the excess liquid ahead of the beam forms at a sufficient rate that there is continuous liquid flow beneath the beam, see Fig. 9c. This results in the formation of a central ridge with accompanying side troughs (12) as shown in Fig. 9e.

In practical applications surface smoothness is of overriding importance and obviously the type of profile in Fig. 9e is highly undesirable. Fortunately, the present experiments show that this effect can be reduced until it is practically negligible, this is attained by selecting appropriate processing parameters. The cross-sectional micrographs in Fig. 3 clearly show the trough-crest effect is minimal at three velocities selected in the range 1.7 to 97.5 cm.s⁻¹ for a beam power of 375 watts. However, by increasing the power to 550 watts the effect is readily apparent, see Fig. 10 and very pronounced when the beam power is 750 watts. Another feature observed at high power levels is a melt zone width far exceeding that predicted by a heat flow model (8). Careful examination of the micrographs suggests this may occur by sideways flow of liquid moving around the beam impingement region where a plasma cavity is formed, see Fig. 9d. In this plan view the heavy arrows show the major flow direction of molten material within the beam depression and the light arrows the sideways flow. This superheated overflowing liquid moves over the hot substrate surface adjacent to the beam and causes further melting in a direction normal to the direction of motion. The net effect of this is an extremely wide melted region near the surface, see Fig. 10.

Transition to the Deep Penetration Mode

In the deep penetration mode, schematically illustrated in Fig. 11, the electron beam penetrates the material to form a plasma cavity which acts as a moving line source. The material ahead of the beam progressively melts, flows through the gap either side and forms a pool bounded by the melting temperature isotherm. The rear portion of this isotherm corresponds to the "ripple profiles" in Fig. 1. Two highly desirable features of

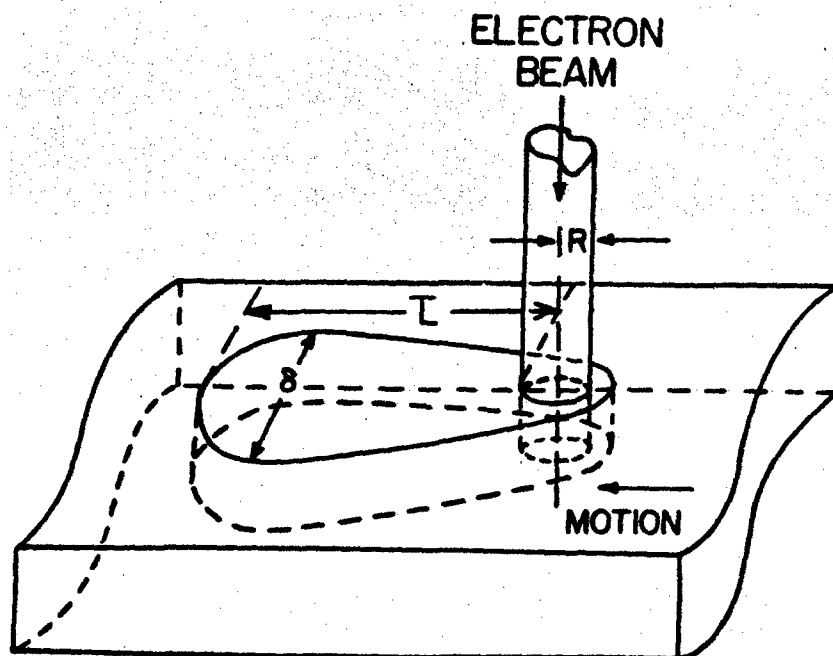


Fig. 11 Schematic diagram showing the deep penetration mode.

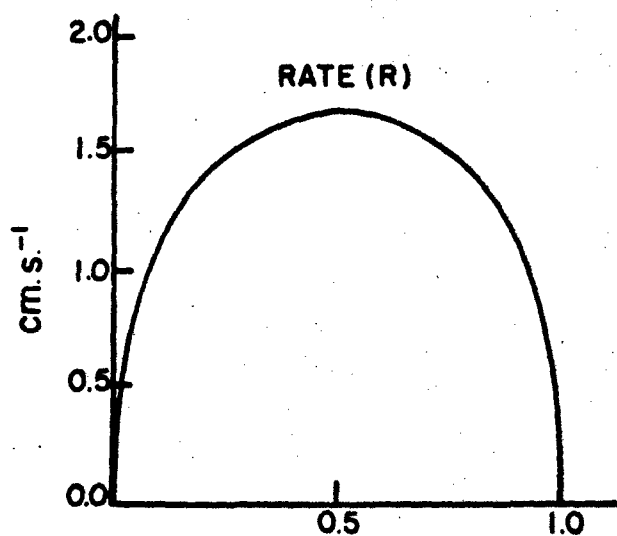
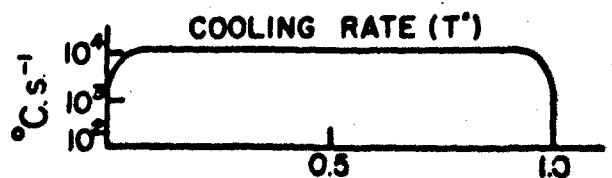
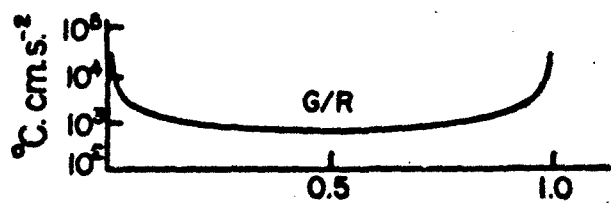


Fig. 12 Values of the rate R , G/R , and cooling rate T' as a function of melt zone width for the deep penetration mode.



this solidification mode are (i) a relatively high cooling rate (5×10^3 to 5×10^4 °C.s⁻¹) and (ii) a high degree of material homogenization due to vigorous hydrothermal mixing and liquid superheating. Computations by Greenwald (13) from a heat flow model are graphically represented in Fig. 12 for a condition where the beam power and velocity are 375 watts and 1.7 cm.s⁻¹. These give values of cooling rate (\dot{T}) the G/R ratio, and the solidification rate (R) across a projection of the solidification interface, i.e. they show the values as they relate to an actual section across the melt zone. For convenience the melt zone width is taken as unity.

By the selection of different parameters for melting the molten pool length can be varied over a wide range. In Table III the molten pool length of 5.6 mm obtained with a beam power of 7.5 kW and velocity of 38.1 cm.s⁻¹ compares with that of ~ 500 μ m for a beam power of 375 watts and velocity of 1.7 cm.s⁻¹. From Table III it is interesting to note that the maximum cooling rate is higher with a high power-high velocity beam than a low power-low velocity beam, i.e., 5×10^4 as compared with 1.4×10^4 °C.s⁻¹.

Microstructure in Deep Penetration Mode

An interesting morphological feature in the transition to the deep penetration mode from the surface melting mode is the rather abrupt change to an equiaxed structure (Fig. 13a) from one with high radial directionality (Fig. 13b). This directionality on a macro-scale results, as previously shown (2,3), from colonies of particularly long-fine scale dendrites.

In comparing the two micrographs in Fig. 13 another interesting feature is the increased preponderance and size of the lightly etched small circular regions. These "white" regions consist of fine-scale martensite/austenite with a particularly high hardness (~ 950 V.H.N.). Previously (2,3) it has been shown that this phase forms at lower cooling rates (10^4 to 10^5 °C.s⁻¹) whereas the darkly etching phase is δ -ferrite retained by cooling at a higher rate ($> 10^5$ °C.s⁻¹). From these considerations it appears then, that appreciable beam penetration results in a phenomenon where a phase characteristic of a lower cooling rate is distributed within a rapidly quenched high temperature phase matrix. This situation can only arise when the temperature distribution within the melt is rather inhomogeneous. In other words, the temperature isotherms rather than being smooth develop irregularities which fluctuate with time and thereby produce erratic variations of \dot{T} at the solidification interface.

In the situation envisaged in Fig. 11 one might anticipate a particularly complex and variable temperature distribution within the melt due to liquid turbulence which would become severe at high flow rates. It should be noted that as the liquid flows through the narrow gap either side the plasma cavity it experiences an extremely high thermal gradient. In the present experiments the gap width is ~ 250 μ m and the temperature difference ($T_V - T_M$) across it is ~ 1500 °C; thus the gradient is $\sim 6 \times 10^4$ °C.cm⁻¹. This will naturally result in appreciable density and viscosity

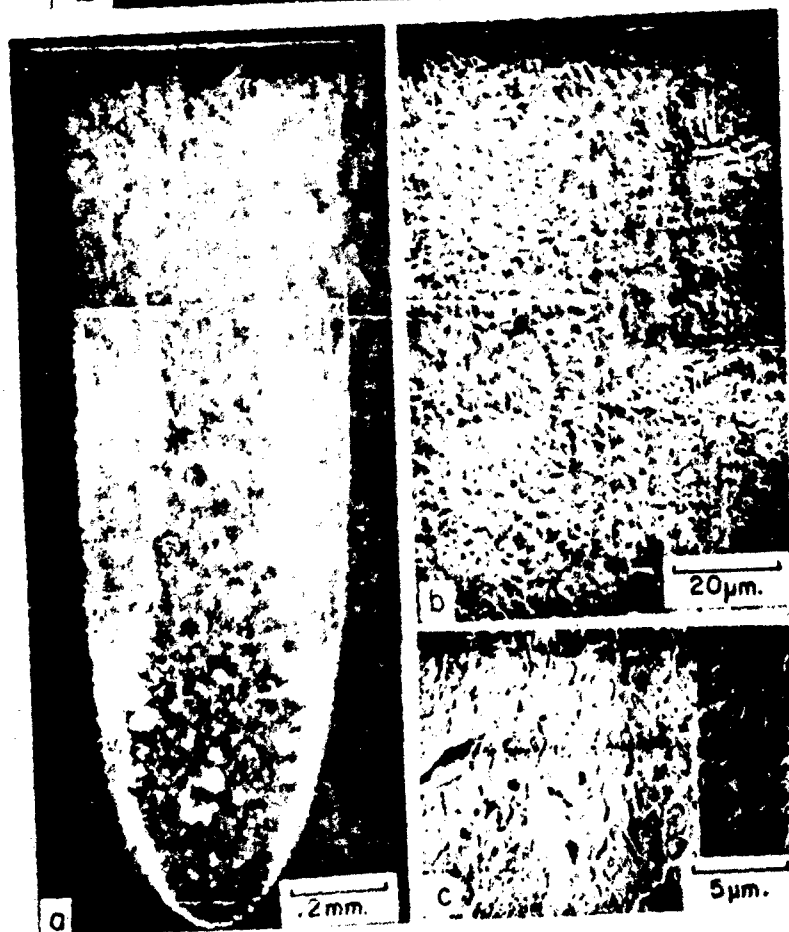
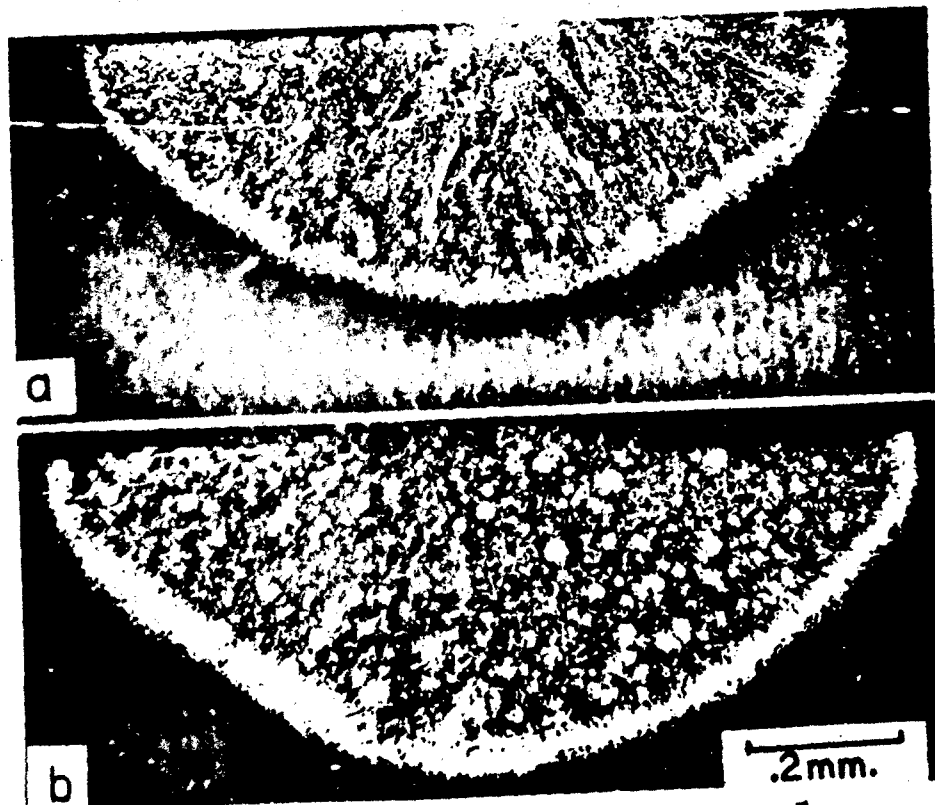


Fig. 13 Microstructural change of melt zone when interaction time is changed from 6×10^{-3} to 8×10^{-3} s.

Fig. 14 Optical cross-sectional view and replica electron micrograph of microstructure in deep penetration mode. Beam power 7.5 kW and beam velocity 37.5 cm.s^{-1} .

gradients arising from the temperature dependence of these physical entities. The existence of liquid turbulence has, in some cases, been observed during the melting process by using a low power stereomicroscopy. Furthermore, it is pertinent to mention that with a beam power of 7.5 kW using a velocity significantly $>37 \text{ cm.s}^{-1}$ results in "blowout" of the molten liquid.

Naturally, liquid turbulence has a chemical stirring effect, as well as facilitating dendrite fragmentation, this doubtless accounts for the formation of an equiaxed structure when beam penetration is appreciable.

An example of deep beam penetration is shown in Fig. 14a where the beam power and velocity are 7.5 kW and 37.5 cm.s^{-1} , pertinent parameters are given in Table III. Since the melt depth is $\sim 2 \text{ mm}$, the linear power density of the line source is $3.75 \times 10^4 \text{ watt.cm}^{-1}$. Again, the light etching phase, which is particularly chemical and electrochemical resistant, is the martensite/austenite phase which has a fairly uniform hardness throughout the melt zone of $\sim 950 \text{ V.H.N.}$ The existence of this phase is confirmatory evidence of a moderately high cooling rate ($> 10^4 \text{ }^\circ\text{C.s}^{-1}$) while the darkly etched phase, in the central zone, is indicative of an even higher cooling rate. The equiaxed cellular microstructure in the martensite/austenite region is revealed in the replica electron micrograph (Fig. 14b). The darkly etched phase is the residual δ -ferrite seen at low magnification in Fig. 14a, which remains untransformed following the ternary peritectic reaction $\delta + \text{liquid} \rightarrow \gamma + \text{carbide}$.

Acknowledgment

The authors are pleased to acknowledge support of this research by the Office of Naval Research, under Contract N00014-78-C-0580.

References

1. E. M. Breinen, B. H. Kear, C. M. Banas and L. E. Greenwald: Superalloys - Metallurgy and Manufacture, p. 345, Claitor's Publishing Division, Baton Rouge, LA., 1976.
2. P. R. Strutt, H. Nowotny, M. Tuli and B. H. Kear. Mat. Sci. and Engr., **36** (1978), pp. 217.
3. Young-Won Kim, P. R. Strutt and H. Nowotny, to appear in Met. Trans.
4. D. Gilbert, M.S. Thesis, University of Connecticut, 1979.
5. T. R. Anthony and H. E. Cline, J. Appl. Phys., **48** (1977), pp. 3888.
6. S. M. Copley, D. Beck, O. Esquivel and M. Bass, pp. 161 in Laser-Solid Interactions and Laser Processing, S. D. Ferris, H. J. Leamy and J. M. Poate, ed.; Amer. Inst. of Physics Conf. Proc., No. 50, New York, 1979.

7. L. E. Greenwald, E. M. Breinen and B. H. Kear, ibid, p. 189.
8. H. E. Cline and T. R. Anthony, J. Appl. Phys., 48 (1977) pp. 895.
9. D. Rosenthal and R. H. Cameron, Trans. Amer. Soc. Mech. Engr., 69 (1947), pp. 961.
10. R. Mehrabian, S. Kou, S. C. Hsu and A. Munitz, pp. 129 in Laser-Solid Interactions and Laser Processing, S. D. Ferris, H. J. Leamy and J. M. Poate, ed., Amer. Inst. of Physics Conf. Proc., No. 50, New York, 1979.
11. H. Matyja, B. C. Giessen and N. J. Grant, J. Inst. Metals, 9 (1968), pp. 30.
12. P. Moore, C. Kim and L. S. Weinman, pp. 221 in Laser-Solid Interactions and Laser Processing, S. D. Ferris, H. J. Leamy and J. M. Poate, ed., Amer. Inst. of Physics Conf. Proc., No. 50, New York, 1979.
13. Private communication, L. E. Greenwald, United Technologies Research Center, East Hartford, Connecticut, June 1979.

Table I

$v \text{ (cm.s}^{-1}\text{)}$	$\lambda \text{ (}\mu\text{m)}$	$T^{\circ} \text{ (}^{\circ}\text{C.s}^{-1}\text{)}$
1.70	1.4	3.9×10^4
4.25	1.2	1.2×10^5
8.50	0.8	2.7×10^5
12.75	0.7	4.4×10^5
38.00	0.5	1.6×10^6
97.50	0.3	5.0×10^6

Measured cellular diameter or secondary dendrite arm spacing as a function of beam/material velocity; the cooling rate is determined from relation of Matyja et al (11).

Table II

v $\text{(cm.s}^{-1}\text{)}$	$\bar{L} \text{ (}\mu\text{m)}$		$T^{\circ} \text{ (cm.s}^{-1}\text{)}$		$D \text{ (}\mu\text{m)}$	
	Obs.	Cal.	Emp.	Cal.	Obs.	Cal.
38.0	10.0	9.9	1.6×10^6	4.5×10^5	108	108
57.5	8.5	6.9	2.7×10^6	1.1×10^6	67	60
76.0	5.0	5.3	3.7×10^6	2.1×10^6	23	34
97.5	3.0	4.1	5.0×10^6	3.8×10^6	18	17

Values of the molten zone length (\bar{L}), cooling rate (T°), and maximum melt depth (D) as a function of beam velocity in region (i), see Fig. 4

Table III

Parameters*	Beam Power and Velocity	
	375 watt	7.5 kW
	1.7 cm.s. ⁻¹	38 cm.s. ⁻¹
Molten Zone Depth**	1200 μ m	2000 μ m
Length (\bar{L})	500 μ m	0.47 cm
Width (δ)	700 μ m	950 μ m
Linear Power Density	3,125 watt/cm.	37,500 watt/cm.

MICROSTRUCTURAL CHARACTERIZATION OF A LASER

MELTED HIGH CARBON STEEL

Mohan Kurup

P. R. Strutt

Department of Metallurgy
University of Connecticut
Storrs, Connecticut 06268

Summary

Laser melting experiments on a high carbon content superplastic steel ($C \sim 1.6$) have been carried out over a wide range of glazing speeds (5 cm.s^{-1} to 125 cm.s^{-1}). Microstructural characterization using optical and electron microscopy revealed that the solubility limit for carbon was extended to an appreciable degree, thus eliminating hypereutectoid carbides. A particularly intriguing result was the observation that fine scale martensite was formed at higher speeds of glazing (25 cm.s^{-1} to 125 cm.s^{-1}). In contrast, no martensite was observed in material melted in the deep penetration mode corresponding to a glazing speed of 5 cm.s^{-1} . However, subsequent quenching into liquid nitrogen resulted in martensite formation. On quenching into liquid nitrogen, no further martensite formation occurred in material glazed at higher speeds.

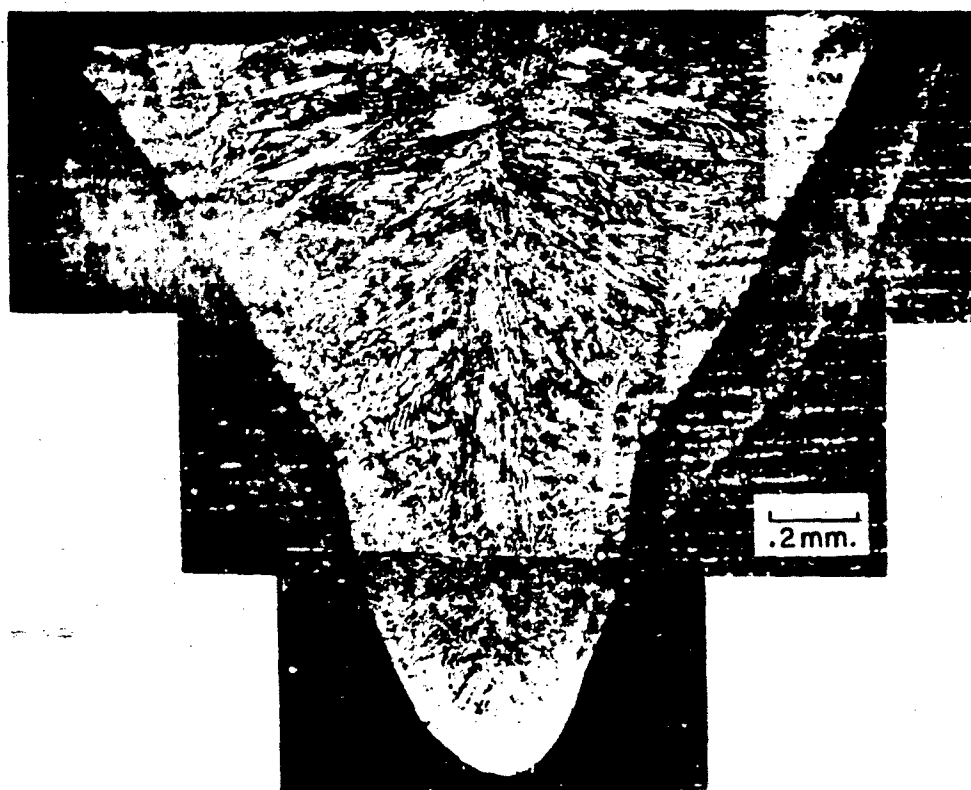


Fig. 1 Schematic diagram showing the microstructure of the deep penetration pass (5 cms.s^{-1}).

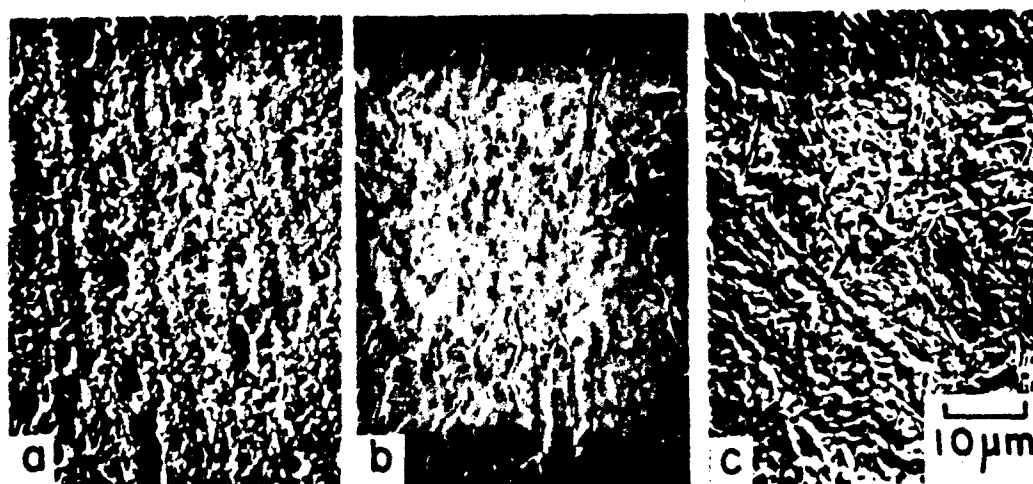


Fig. 2 a. Substrate showing coarse carbides and their directionality
 b. Melt zone revealing the complete dissolution of carbides with carbide precipitation along grain boundaries
 c. Martensitic structure formed in the melt zone of 2b after liquid nitrogen quench

Introduction

Recent experiments on laser/electron beam surface melting of tool steels have shown that at high solidification rates there is an extension of the solubility limit and dissolution of all carbide phases (1). These results are comparable with those obtained by splat quenching (2) and by laser glazing other materials (3). In view of this, a study was undertaken on laser-glazing an ultra high carbon superplastic steel. The results obtained by detailed microstructural examination and subsequent quenching will now be presented and summarized in this paper.

Experimental Procedure

The specific ultra high carbon steel used in the study was originally investigated by Wadsworth and Sherby (4) who showed that it became superplastic following appropriate thermomechanical processing. The composition of the steel in weight percent is as follows: 1.6C, 1.5Cr, 0.5Mn, 0.15Si, Bal Fe. Actual laser surface melting was carried out at United Technologies Research Center, East Hartford, Connecticut, using a 5.1 kW continuous CO₂ laser beam with a 0.51 mm beam diameter. The surface of the material was scanned for a range of beam velocities, ranging from 5 to 125 cm.s⁻¹. Metallographic observations were carried out both on cross-sections and longitudinal sections. These were examined using both optical and scanning electron microscopy. In addition, microhardness measurements were performed and related to microstructural observations.

Results and Discussion

The approximate Ms temperature of the steel, as determined by the relation of Andrews (5) is -153°C. As shown by Wadsworth and Sherby (4), this material, prior to thermomechanical processing, has a coarse pearlitic structure with pro-eutectoid cementite at the grain boundaries. Following thermomechanical processing, the material exhibits a strong directionality of carbides in the rolling direction (4), see Fig. 2a.

The effect of laser surface melting, at all beam velocities (ranging from 5 to 125 cm.s⁻¹), is to completely dissolve the original carbide structure and remove any evidence of the texture in the rolling direction. In terms of microstructural features, however, the laser melted zone formed at the lowest beam velocity (5 cm.s⁻¹) appreciably differs from those formed at the high beam velocities. In the low magnification composite micrograph in Fig. 1, the convex downward protruberance at the bottom of the zone is clear evidence of beam penetration and shows that melting occurs in the deep penetration mode. As might be expected the cooling rate is higher below the tip of the plasma cavity, the result of this is evident in Fig. 1, where the microstructure in the protruberance is considerably more refined. The overall noticeable effect in Fig. 1 is the strong radial directionality and at higher magnification this is seen to arise from long

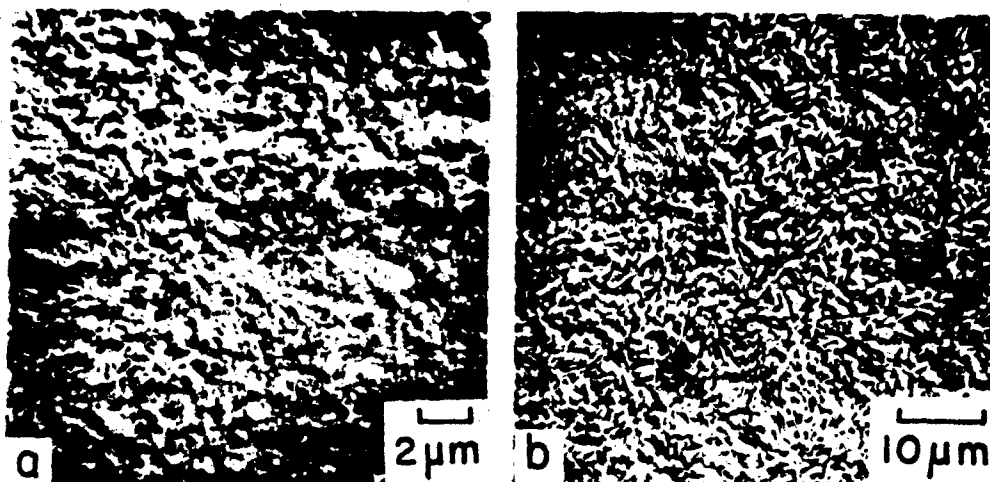


Fig. 3 Microstructure corresponding to high beam velocities (125 cms.s^{-1} and 25 cms.s^{-1}). a) Extremely fine martensite b) Clear martensitic structure corresponding to a velocity of 25 cms.s^{-1}

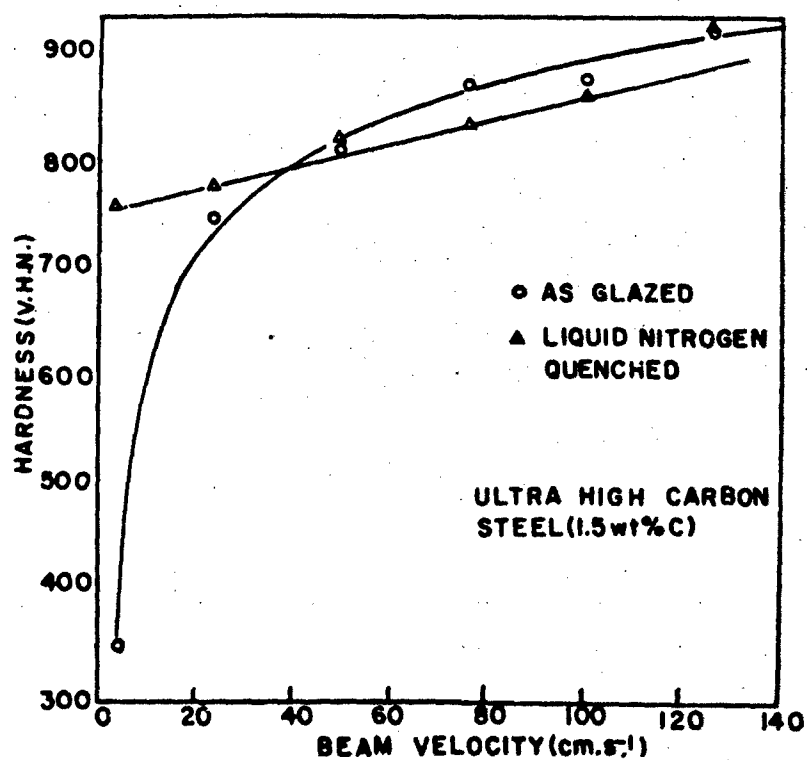


Fig. 4

cellular boundaries decorated with continuous carbides, see Fig. 2b. The interior of the relatively elongated cells of retained austenite appear to be relatively featureless with no evidence of martensite; hardness measurements show this microstructure to be particularly soft (V.H.N. ~ 350). Based on computer calculations of a moving line source, the mean cooling rate for the melt zone in Fig. 1 is $\sim 2 \times 10^4 \text{ } ^\circ\text{C.s}^{-1}$ (6).

Another interesting feature in Fig. 1 is that surrounding the melt zone there is a transition region consisting of fine grained austenite together with some undissolved carbide particles. The heat affected zone is also interesting in that it is microstructurally harder (850 V.H.N. as compared with 374 V.H.N.). Considering again the melted region, it was found that liquid nitrogen quenching produced the martensitic microstructure shown in Fig. 2c which has an average hardness of 758 V.H.N., see Fig. 4 and Table I. This type of hardening is similar to that obtained by Wadsworth and Sherby (4) in the as-thermomechanically processed material.

Table I

Vickers Diamond Pyramid Hardness of As
Glazed Laser Zone in Ultra High Carbon Steel

<u>Speed of Glazing</u> <u>cm/sec</u>	<u>Fusion</u> <u>Zone</u>	<u>Heat Affected</u> <u>Zone</u>	<u>Substrate</u>
127 (as glazed)	913	775	381
127 (L.N.Q*)	918	644	362
102 (as glazed)	874	755	373
102 (L.N.Q.)	860	712	376
76 (as glazed)	868	814	373
76 (L.N.Q.)	828	827	376
51 (as glazed)	811	827	373
51 (L.N.Q.)	821	832	376
25 (as glazed)	745	946	373
25 (L.N.Q.)	775	953	376
51 (as glazed)	350	1024	390
	758	1130	404

* L.N.Q. = Liquid Nitrogen Quenched (-196°C)

In contrast to the melted zone formed at the lowest cooling rate ($\sim 2 \times 10^4 \text{C.s}^{-1}$), all material formed using a beam velocity $> 25 \text{ cm.s}^{-1}$ was martensitically strengthened with the actual hardness as a function of velocity, see Fig. 4. Interestingly no appreciable hardness increase was determined in any instance by subsequent quenching into liquid nitrogen. The longitudinal section micrograph in Fig. 3b clearly shows the martensitic structure in the material melted with a beam velocity of 25 cm.s^{-1} (calculated cooling rate $\sim 3 \times 10^4 \text{C.s}^{-1}$). Experiments showed that the scale of martensitic microstructure progressively decreased with increasing cooling rate. At the highest beam velocity (125 cm.s^{-1}) the microstructure was particularly refined and homogeneous as shown in Fig. 3a. This highly convoluted fine filamentary martensitic structure produces the maximum attainable hardening, see Fig. 4.

In summary, it is particularly interesting to show that a hardness comparable to that obtained by conventional treatment can be attained without the usual quenching in liquid nitrogen. A similar result was obtained on splat quench iron-carbon-silicon alloys by Ruhl and Cohen (2). However these authors did not investigate the effect of cooling rate or study the microstructure. The martensite formed by rapid quenching differs morphologically from that normally obtained and its scale is particularly sensitive to the cooling rate. The mechanisms involved obviously require a very detailed investigation, since for example, the cooling rate might control martensite nucleation either directly through the degree of supercooling or the transformation strains thereby produced.

Acknowledgement

It is a pleasure to acknowledge support of the present research by the Office of Naval Research under Contract N00014-78-C-0580.

References

1. P.R. Strutt, H. Nowotny, M. Tull, and B.H. Kear: Materials Science and Engineering; **36** (1978), pp. 217.
2. R.C. Ruhl and Cohen; Materials Science and Engineering, **1** (1967), pp. 315.
3. B.H. Kear, E.M. Breinan, and L.E. Greenwald; Metals Technology, **6** (1979), 121.
4. J. Wadsworth and O.D. Sherby; Journal of Materials Science, **13** (1978), 2645.
5. E.R. Petty; Martensite, Longmans Ltd., London (1970).
6. Private communication, L.E. Greenwald, United Technologies Research Center, East Hartford, Connecticut, June 1979.

LASER SURFACE TREATMENT OF PSEUDO-BINARY Fe-TiC ALLOYS

D. Gilbert, P. R. Strutt and H. Nowotny

Department of Metallurgy, University of Connecticut,
Storrs, CT 06268

Summary

Recent studies have been made on Fe-TiC alloys whereby comparison of microstructure and hardness have been made between conventionally solidified material and zones of material that had been rapidly quenched following laser surface melting. Results indicate that while the parent material exhibits a hardness of 500 to 600 KHN with a microstructure characterized by a coarse dendritic carbide distribution in a eutectic matrix, the melt zones exhibited a hardness of 1200 to 1350 KHN associated with a refined carbide distribution in a modified eutectic microstructure. The eutectic composition of the pseudo-binary Fe-TiC phase diagram was determined from measurements of the volume fraction carbide. There is a shift in the eutectic composition of the laser melt zone as compared with the parent material which can be explained in terms of the effect of rapid quenching. Lattice parameter measurements have been made on material powdered from both melt zone and parent material. The lattice parameter of the TiC is unaffected by the laser surface melting, while that of the iron is expanded slightly, indicating an extension in the solubility of TiC in the Fe of the melt zone.

Introduction

One of the potentially most exciting applications of laser surface melting is its application for developing new iron-base materials. Stimulus for persuing basic research on laser-glazing of cemented carbides, for example, is the possibility of exploiting the unique features of ultra-refined microstructures. Traditionally, a method of producing an extremely hard material is to embed a high volume fraction of carbide particles in a binder material. This approach, unfortunately, has the severe drawback that hardness is obtained at the sacrifice of other highly desirable characteristics, such as fracture toughness. An alternative to this, facilitated by the new rapid solidification technique, is to exploit the high hardness of an ultra-refined carbide/metal lamellar structure, as was recently demonstrated with a tantalum carbide-cobalt alloy (1). Using this approach one not only substantially increases the hardness but also obtained a highly homogeneous material which, one might anticipate, would have improved fracture toughness.

In view of the proceeding considerations, a study was undertaken on a series of Fe-TiC alloys.

Experimental Procedure

This paper describes a study on alloys with compositions in the pseudo-binary Fe-TiC alloy system. The three compositions selected had 5.3, 17.6 and 33.3 atomic % titanium carbide. The alloy ingots, of about 200 gm. weight, were prepared from high purity Fe, Ti, and C by melting and casting in an argon arc furnace. Sectioning and subsequent microscopic examination revealed that the 5.3 atomic % alloy was hypoeutectic, while the 17.6 and 33.3 atomic % alloys were hypereutectic. This result was expected since Jellinghaus (2) had determined that the Fe-Ti-C pseudo-binary has an eutectic composition of about 12 atomic %.

Hardness studies of the parent material revealed that the hardness of the 5.3 and 17.6 at. % TiC alloys were identical (averaging between 500 to 550 KHN) while that of the 33.3 at. % TiC alloy was only slightly higher (averaging 550 to 600 KHN).

The X-ray powder diffraction patterns revealed only two phases, bcc ferrite and fcc TiC, and that the lattice parameters of each phase were the same for each alloy. These values are:

<u>Phase</u>	<u>Lattice Parameter $\overset{\circ}{\text{\AA}}$</u>
ferrite	2.86 ₆
TiC	4.32 ₀

From these lattice parameter measurements, it is evident that the ferrite phase can contain only small amounts of Ti and C since within the experimental accuracy, the observed lattice parameter

is the same as that for pure iron. However, since no change in the lattice parameter for iron is expected until the Ti and C contents exceed .38 and .018 at. % respectively (3), no more than these amounts are dissolved in the ferrite.

The lattice parameter found for TiC indicates a slight carbon deficiency (about 4 at.%), although Rudy (4) has indicated that such a deficiency commonly occurs. Since the amounts of Ti and C in the starting material were sufficient to produce the stoichiometric compound TiC, one concludes that some carbon has been lost during alloy fabrication.

X-ray fluorescence studies performed on the SEM revealed that the iron is segregated to the interdendritic regions, while the dendrites contain titanium. Fig. 1 shows this effect for the material of composition at 33.3 at. % TiC. The large dendrite particles were shown to be titanium carbide, while the matrix was shown to be a ferrite/TiC eutectic.

Results

The laser glazing experiments were performed by scanning the specimen surface with a 3 kW continuous CO₂ laser with a 0.51 mm spot diameter. Since conventionally cast material contains particularly large carbide particles the material was homogenized by slowly scanning the surface at 12.7 cm/sec to obtain melting to a depth of about 500 μ m. Following this another pass at 50.8 cm/sec was made to obtain a rapidly solidified zone of melt depth about 130 μ m.

The microstructure of the hypoeutectic alloy (5.3 at. % TiC) before laser glazing is shown in Fig. 2a. From Fig. 2b it is readily apparent that laser glazing results in the formation of a microstructure on an exceedingly fine scale as compared with that in Fig. 2a. In Fig. 2b the region melted by the second laser pass extends from the top to slightly below the middle of the micrograph. The difference in microstructural scale between the two regions in Fig. 2b clearly shows the slower cooling rate in the initial homogenizing laser pass. At a higher magnification of the upper region in Fig. 2b the microstructure in the replica electron micrograph (Fig. 2c) is seen to consist of a cellular ferrite matrix with an intercellular fine filamentary eutectic structure. The average diameter of the ferrite cells is about 1.5 μ m. The hardness of the second laser melted region is quite uniform with an average value of 800 KHN.

We now consider the hypereutectic composition alloys whose microstructure following laser glazing are shown in Fig. 3 for the alloy containing 33.3 at. % TiC. In this case proeutectic dendrites form which have a mean secondary dendrite arm spacing of about 1.5 μ m in the case of the deep melt zone. Using the empirical relation of Matyja, Glessen and Grant (5) relating dendrite arm spacing with cooling rate the cooling rate in this case is about 4×10^4 K/sec. The proeutectic dendrites are surrounded by a cellular matrix (mean cell diameter about 3 μ m). These

features are seen in Fig. 3. The matrix consists of a cellular structure TiC/ferrite eutectic composed of equiaxed ferrite particles surrounded by a continuous carbide network.

The transition region between the arc-cast material and the deep laser zone is characterized by large proeutectic TiC particles of the parent material (which have not melted to any appreciable extent) surrounded by a matrix which was melted by the laser glazing process. These features are depicted in Fig. 4a. Solidification conditions for the matrix favor the formation of large cells of lamellar eutectic microstructure, as shown in Fig. 4b.

The microstructure of the shallow melt zone is qualitatively similar to that of the deeper homogenizing pass but is more highly refined. The proeutectic TiC particles have a mean secondary dendrite arm spacing of $0.75 \mu\text{m}$ and the mean cell diameter is $1.5 \mu\text{m}$. Again, from the empirical relation between dendrite arm spacing and cooling rate (5), the cooling rate is approximately $4 \times 10^5 \text{K/sec}$.

Hardness tests performed on the hypereutectic alloys show that the maximum hardness in each case occurs at the interface between the deep melt zone and the parent material. For the 33.3 at. % TiC alloy, the hardness in the interfacial region averages between 1350 and 1400 KHN. The hardness in the remainder of the melt zone is quite uniformly 1200 KHN. These values compare with an average hardness of 600 KHN for the parent material.

X-ray powder diffraction measurements for each sample revealed the presence of the same two phases as were found in the parent material. While the lattice parameter of the TiC is unchanged by the melting process, that of the ferrite exhibits a small increase. Although this increase is at the limits of sensitivity of the technique (in view of the broadness of the lines), the change in both direction and magnitude of the lattice parameter is reproducible. This is consistent with an increase in the solubility of Ti in ferrite of about 3 at % or an increase in solubility of C in ferrite of about 4 at %. More diffuse X-ray diffraction lines are seen for iron from the melt zone (with respect to iron from the parent material) and this arises from the smaller ferrite grain size and residual stresses in the melt zone characteristic of rapid quenching.

Composition (at. % TiC)	Lattice Parameter A ^o			
	ferrite		TiC	
	parent	melt	parent	melt
33.3	2.86 ₆	2.87 ₅	4.32 ₅	4.32 ₅
17.6	2.86 ₆	2.87 ₃	4.32 ₆	4.32 ₆
5.3	2.86 ₆	2.87 ₀	4.32 ₀	4.31 ₅

Discussion

It is interesting to note that the cellular eutectic structure between the carbide particles between the melt zones was similar in appearance to the eutectic structure observed by Sare and Honeycombe in Fe-Mo-C alloys (6). This eutectic is composed of equiaxed ferrite particles surrounded by a continuous carbide network. Such a eutectic structure is quite different from the refined lamellar eutectic observed in laser surface melted Co-Ta-C alloys studied by Breinan et. al. (1).

A significant difference between the parent and rapidly solidified material is a change in the morphology of the eutectic microconstituent. The eutectic occurs as the typical lamellar form in the parent material. However, the laser melt zones contain a cellular eutectic structure composed of equiaxed ferrite particles surrounded by a continuous carbide network. A similar eutectic structure has been observed in splat quenched Fe-Mo-C alloys by Sare and Honeycombe (6). The occurrence of the cellular eutectic in laser melted Fe-Ti-C alloys was unexpected since laser melts of a similar system Co-Ta-C contain the lamellar eutectic.

Acknowledgement

It is a pleasure to acknowledge support for the present study by the Office of Naval Research on Contract N00014-78-C-0580.

References

1. Breinan, E. M., Kear, B. H., Banas, C. M., and Greenwald, L.E. "Surface Treatment of Superalloys by Laser Skin Melting" p. 435, in Superalloys: Metallurgy and Manufacture, ed. by B. H. Kear, Claitor's Pub. Div., Baton Rouge, LA (Sept. 1976)
2. Jellinghous, W. "Beitrag zum Dreistoffsystem Eisen-Titan-Kohlenstoff und zur Verbindung Fe_2Ti " in Archiv für das Eisenhüttenwesen, 40, (1969), p. 483.
3. Pearson, W. B. Handbook of Lattice Spacings and Structures of Metals and Alloys, p. 661 and 919, Pergamon Press, London, 1958.
4. Rudy, E. Ternary Phase Equilibria in Transition Metal-Boron-Carbon-Silicon Systems, Part V: Compendium of Phase Diagram Data. Air Force Materials Lab. W-P AFB, Ohio, AFML-TR-65-2 Part V, p. 160 June 1969 .
5. Fleming, M.C. Solidification Processing, p. 148, McGraw-Hill, New York, N.Y. (1974).
6. Sare, I.R. and Honeycombe, R.K.W. "Structure Produced by Rapid Quenching of Molybdenum Steels" p. 87 in Rapidly Quenched Metals, Second International Conference, ed. by N.J. Grant and B.C. Giessen, MIT Press, Cambridge, MA. 1976.

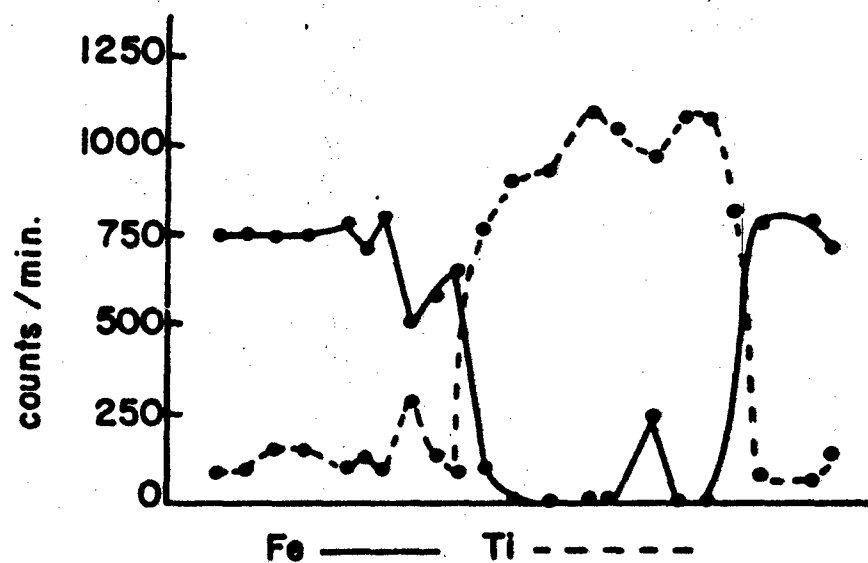


Fig. 1 X-ray fluorescence studies demonstrating segregation of iron to the matrix and Ti to the second phase dendritic particles in 33.3 at. % TiC alloy.

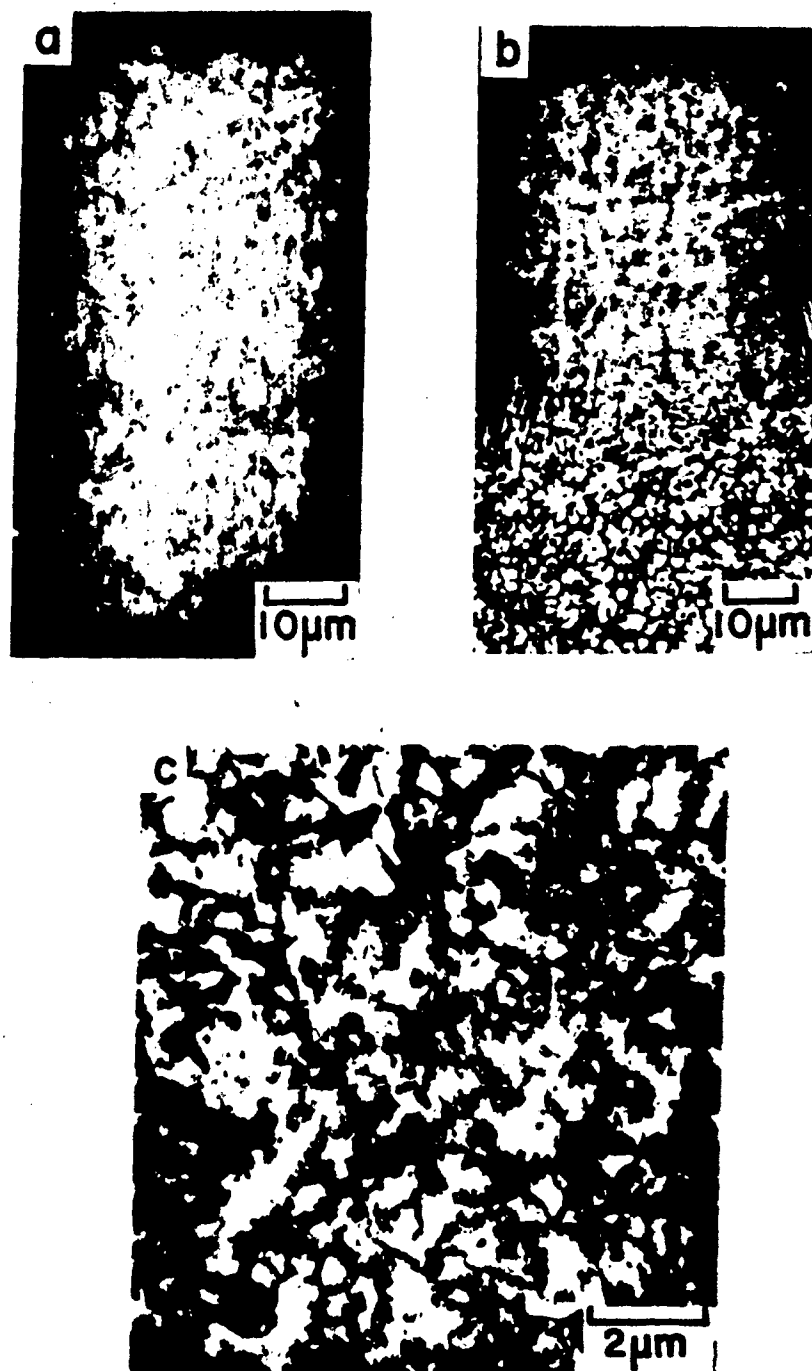


Fig. 2 a. Microstructure of the 5.3 at. % TiC alloy before laser glazing.
 b. Result of laser glazing the 5.3 at. % TiC alloy. The second laser pass extends from the top to slightly below the middle.
 c. The microstructure of the second melt zone.

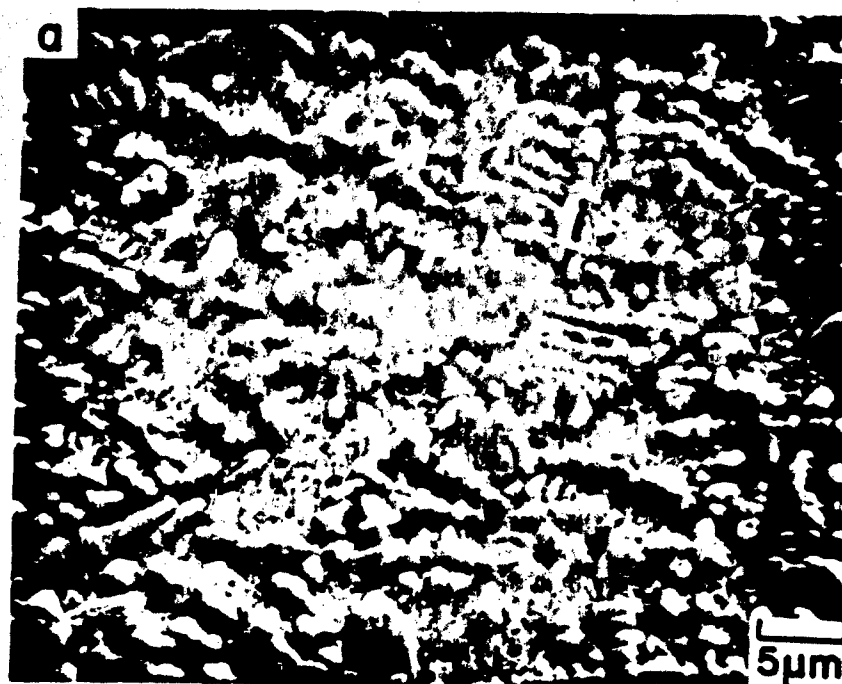


Fig. 3 a. Microstructure of the melt zone in the 33.3 at. % TiC alloy.
 b. Higher magnification of interdendritic region showing cellular structure in matrix.



Fig. 4a The transition region between the arc-cast material and the deep laser melt zone.

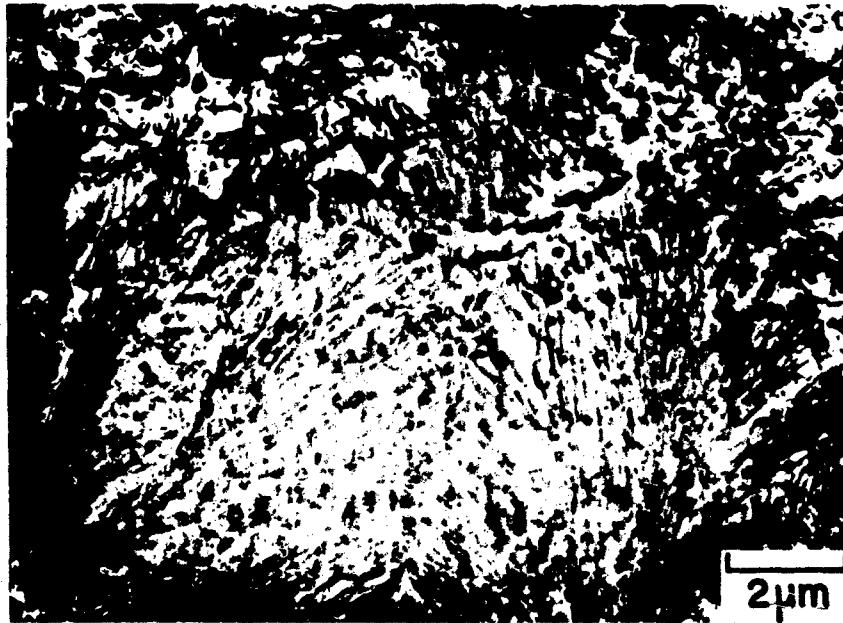


Fig. 4b Higher magnification micrograph of dark paths in 4a revealing fine lamellar.

REPORT DOCUMENTATION PAGE		READ INSTRUCTIONS BEFORE COMPLETING FORM
1. REPORT NUMBER	2. GOVT ACCESSION NO.	3. RECIPIENT'S CATALOG NUMBER
4. TITLE (and Subtitle) SURFACE HARDENING BY LASER SKIN MELTING		5. TYPE OF REPORT & PERIOD COVERED First Yearly Report, July 1979
		6. PERFORMING ORG. REPORT NUMBER
7. AUTHOR(s) Peter R. Strutt		8. CONTRACT OR GRANT NUMBER(s) N00014-78-C-0580
9. PERFORMING ORGANIZATION NAME AND ADDRESS Metallurgy Department University of Connecticut Storrs, CT 06268		10. PROGRAM ELEMENT, PROJECT, TASK AREA & WORK UNIT NUMBERS
11. CONTROLLING OFFICE NAME AND ADDRESS Office of Naval Research Arlington, Virginia 22217		12. REPORT DATE July, 1979
		13. NUMBER OF PAGES 57
14. MONITORING AGENCY NAME & ADDRESS (if different from Controlling Office)		15. SECURITY CLASS. (of this report) Unclassified
		15a. DECLASSIFICATION/DOWNGRADING SCHEDULE
16. DISTRIBUTION STATEMENT (of this Report) Unlimited		
17. DISTRIBUTION STATEMENT (of the abstract entered in Block 20, if different from Report)		
18. SUPPLEMENTARY NOTES		
19. KEY WORDS (Continue on reverse side if necessary and identify by block number)		
20. ABSTRACT (Continue on reverse side if necessary and identify by block number) A basic study has been initiated on the microstructural characterization of rapid quenched iron-base alloys produced by electron beam-glazing and laser-glazing. The quantitative effect of processing parameters (i.e., beam velocity, power, etc.) on melt zone geometry have been determined using M2 tool steel as a reference material. The conditions range from superficial surface melting with correspondingly high cooling rates ($\sim 5 \times 10^6 \text{ }^\circ\text{C.s}^{-1}$) to the deep penetration mode, with a cooling rate of $\sim 10^4 \text{ }^\circ\text{C.s}^{-1}$. The comparison of electron beam and laser-glazing was particularly striking, since the power efficiency in surface		

DD FORM 1 JAN 73 1473

EDITION OF 1 NOV 68 IS OBSOLETE

Unclassified

SECURITY CLASSIFICATION OF THIS PAGE (When Data Entered)

Similar to 1600 highest centrifuge 5

Similar to 160002

~~Unclassified~~

SECURITY CLASSIFICATION OF THIS PAGE(When Data Entered)

melting was ten times greater using an electron beam. Furthermore, electron beam glazing produced (i) a uniform and smooth surface, (ii) a constant depth of melting, and (iii) a homogeneous microstructure. These highly desirable features were not achieved to the same degree in the laser-glazing experiments.

It was demonstrated that the degree of microstructural refinement in Fe-TiC alloys produced a significant improvement in hardness. For example, in one alloy, laser glazing increased the hardness from 550 K.H.N. to 1350 K.H.N. In a high carbon steel (~ 1.5 wt% C) the effect of rapid quenching was to dramatically increase the M_s temperature. The scale of the martensitic structure was found to be sensitive to the quenching rate. At the highest rate ($\sim 5 \times 10^3$ °C.s⁻¹) an exceedingly fine scale filamentary martensite/ferrite microstructure produced the highest degree of hardness (~ 950 V.H.N.).

~~Unclassified~~

SECURITY CLASSIFICATION OF THIS PAGE(When Data Entered)

INSTITUTE OF MATERIALS SCIENCE

The Institute of Materials Science was established at The University of Connecticut in 1966 in order to promote the various fields of materials science. To this end, the State of Connecticut appropriated \$5,000,000 to set up new laboratory facilities, including approximately \$2,150,000 for scientific equipment. In addition, an annual budget of several hundred thousand dollars is provided by the State Legislature to support faculty and graduate student salaries, supplies and commodities, and supporting facilities such as various shops, technicians, secretaries, etc.

IMS fosters interdisciplinary graduate programs on the Storrs campus and at present is supporting five such programs in Alloy Physics, Biomaterials, Crystal Science, Metallurgy, and Polymer Science. These programs are directed toward training graduate students while advancing the frontiers of our knowledge in technically important areas.